LIMNOLOGY
and
OCEANOGRAPHY: METHODS

*Limnol. Oceanogr.: Methods* 12, 2014, 617–636


# Time response of oxygen optodes on profiling platforms and its dependence on flow speed and temperature

*Henry C. Bittig*, Björn Fiedler, Roland Scholz, Gerd Krahmann, and Arne Körtzinger*
Helmholtz Centre for Ocean Research Kiel (GEOMAR), Kiel/Germany

## *Abstract*

The time response behavior of Aanderaa optodes model 3830, 4330, and 4330F, as well as a Sea-Bird SBE63 optode and a JFE Alec Co. Rinko dissolved oxygen sensor was analyzed both in the laboratory and in the field. The main factor for the time response is the dynamic regime, i.e., the water flow around the sensor that influences the boundary layer's dynamics. Response times can be drastically reduced if the sensors are pumped. Laboratory experiments under different dynamic conditions showed a close to linear relation between response time and temperature. Application of a diffusion model including a stagnant boundary layer revealed that molecular diffusion determines the temperature behavior, and that the boundary layer thickness was temperature independent. Moreover, field experiments matched the laboratory findings, with the profiling speed and mode of attachment being of prime importance. The time response was characterized for typical deployments on shipboard CTDs, gliders, and floats, and tools are presented to predict the response time as well as to quantify the effect on the data for a given water mass profile. Finally, the problem of inverse filtering optode data to recover some of the information lost by their time response is addressed.

Dissolved oxygen has an unmatched history in ocean observation among all chemical ocean parameters. It belongs to the most commonly measured chemical quantities, and the most mature chemical sensors are available for dissolved oxygen (Johnson et al. 2007). Traditionally, these were Clark-type electrochemical sensors, one of the most mature versions of which is the widely used Sea-Bird SBE43 electrode. They feature a fast time response, which make them suitable for profiling applications like ship-based CTD surveys. However, their major drawback is the need for recalibrations or in situ reference samples on timescales of weeks to months since they lack long-term stability.

More recently (as early as the late 1990s), optical oxygen sensors for marine applications emerged as an alternative (Klimant et al. 1995; Demas et al. 1999). Unlike electrodes, these optodes do not consume oxygen so their absolute response is not flow sensitive (Tengberg et al. 2006). However, their response rate to a changing $O_2$ level definitely is flow sensitive.

Optodes have been shown to be stable during deployments of several years (e.g., Körtzinger et al. 2005), but calibrations may change between laboratory characterization and deployment (e.g., Bittig et al. 2012). Whereas recalibrations are, in principle, feasible during ship-based CTD surveys, they pose a significant challenge for newer and more innovative profiling observation platforms, such as floats and gliders. Especially these autonomous and unattended platforms call for cost-effective, energy-efficient, long-term-stable, accurate, robust, and reliable sensors. Whereas none of today's commercial optodes meet all requirements, they fulfill many criteria and belong to the standard configuration of many instruments, e.g., Argo-$O_2$ floats (Gruber et al. 2010).

However, a major concern with the application of optodes on profiling platforms is the comparatively slow response attributed to these sensors. Little is known about the actual in situ time response and the specific effects on the data. We aim to fill this gap with a systematic study of five commercially available optical oxygen sensors.

The main goal is the quantification of the time response and its effect under field conditions. The two factors influencing the time response are the flow speed in front of the sensor and the temperature. Two sets of laboratory experiments were performed to separate them: First, the flow speed dependence was investigated at constant temperature, and second, the temperature dependence was analyzed under constant flow regime. The findings from these experiments were then validated against field deployments on today's major oceanographic platforms: shipboard CTDs, gliders, and floats. The flow speed turned out to be of prime importance and response

*Corresponding author: E-mail: hbittig@geomar.de

***Acknowledgments***

Full text appears at the end of the article.

DOI 10.4319/lom.2014.12.617

times τ well below 10 s are easily obtained if the sensors are pumped.

## Materials and procedures

### Optode descriptions

The sensing principle of optical oxygen sensors is based on the dynamic or collisional quenching of luminescence by oxygen. After a luminophore has been excited with short-wavelength light, it may return to its ground state either through radiationless de-excitation or through luminescence, i.e., emission of light with longer wavelength. If oxygen is present, $O_2$ can collide with the luminophore and absorb the excess energy of the excited state thereby quenching luminescence. Both the luminescence intensity $I$ and the excited state lifetime Λ are reduced by collisional quenching, and their behavior is described by the Stern-Volmer equation (Eq. 1)

$$\frac{I_0}{I} = \frac{\Lambda_0}{\Lambda} = 1 + K_{SV} \cdot pO_2 \quad (1)$$

where $pO_2$ is the partial pressure of $O_2$, $K_{SV}$ is the Stern-Volmer constant, and $I_0$ and $\Lambda_0$ are the intensity and lifetime in absence of oxygen, respectively.

Using an intensity-modulated excitation light source, the luminescence emission is modulated, too, but phase shifted due to the finite lifetime of the excited state according to Eq. 2

$$\tan \varphi = 2\pi \cdot f \cdot \Lambda \quad (2)$$

with $f$ being the modulation frequency and φ the phase shift. The calibration coefficients relate the phase shift φ (and temperature $T$) as measured quantity to the oxygen partial pressure $pO_2$ as quantity of interest. (Commonly, temperature-dependent parametrizations for $\Lambda_0(T)$ and $K_{SV}(T)$ [see Eq. 1] are applied.)

All sensors used in this study (Table!1) have been thoroughly calibrated using Winkler-based multi-point laboratory (Bittig et al. 2012) or in situ calibrations (details can be found in the appendix). The partial pressure $pO_2$ is the quantity determining equilibrium between different media, i.e., the sensing membrane and the bulk environment, and will be used for most of the discussions. However, the oxygen concentration $c(O_2)$ is used for all field applications. Both parameters essentially carry the same information and can be converted using the Henry's law solubility constant $\alpha(O_2)$/μmol kg$^{-1}$ Pa$^{-1}$.

The oxygen optode models 3830, 4330, and 4330F (Aanderaa Data Instruments AS) as well as the SBE63 optode (Sea-Bird Electronics) are based on a luminescent platinum porphyrine complex immersed in a silicone membrane (PSt3 membrane, PreSens GmbH). The membrane is mounted on an optical window. Whereas the membrane is exposed directly to the ambient medium for the Aanderaa optodes, the SBE63 is designed for use in a CTD's pumped flow path. Therefore, the optical window is contained within a plenum, i.e., a flow-through mount, and is not exposed to the ambient medium without it being pumped through the plenum.

The Rinko optical oxygen sensor (JFE Alec Co. Ltd) uses the same dynamic quenching principles but different materials. Its luminophore is coated onto the optical window (transparent acrylic resin PMMA) which is open to the ambient medium.

### Time response quantification

For quantification of the time response, two measures are used. The first one is a response time τ, which is the standard way of characterization (Tengberg et al. 2006; Sea-Bird Electronics 2012). It corresponds to the time constant of an exponential step response. The second is based on a diffusional model of the optode–water interface. It consists of two stationary layers, one for the sensing membrane and one for the aqueous boundary layer in front of the membrane.

Beause oxygen diffusivity $D$ in water is about three orders of magnitude smaller than the kinematic viscosity $\nu$ (Schmidt number $Sc = \nu/D \approx 500$), oxygen diffusion occurs entirely within the inner 10% of the velocity boundary layer where the flow is considerably decelerated by friction. Advection can thus be neglected inside the diffusive boundary layer, and the layer can be treated as stagnant.

The model is based on Fickian diffusion and uses temperature-dependent parameterizations for the diffusivity $D(T)$ and solubility $S(T)$ in both layers. The sensing membrane thickness $l_M$ is prescribed while the stagnant, diffusive boundary layer thickness $l_L$ is adjusted to match the observation.

The model is illustrated in Fig.!1a and step response curves $h(t)$ for different $l_L$ values are shown in Fig. 1b.

The smaller the boundary layer, the steeper the gradient between ambient medium and sensing membrane and thus the stronger the $O_2$ supply to the sensor. In consequence, the sensor's time response becomes faster. Details of the diffu-

**Table 1.** Optode properties and manufacturer specifications.

| Optode manufacturer | Optode model | Flow regime | Luminophore matrix | Response time τ/s |
|---|---|---|---|---|
| Aanderaa | 3830/4330 | diffusive | PreSens PSt3 | 25 s |
| Aanderaa | 4330F | diffusive | PreSens PSt3* | 8 s |
| Sea-Bird | SBE63 | pumped | PreSens PSt3 | 6 s |
| JFE Alec Co. | Rinko | diffusive | PMMA coating | (0.4 s)† |

*The 4330F model uses a thinner version of the PSt3 membrane without optical isolation.
†The manufacturer states a gas phase response time only.

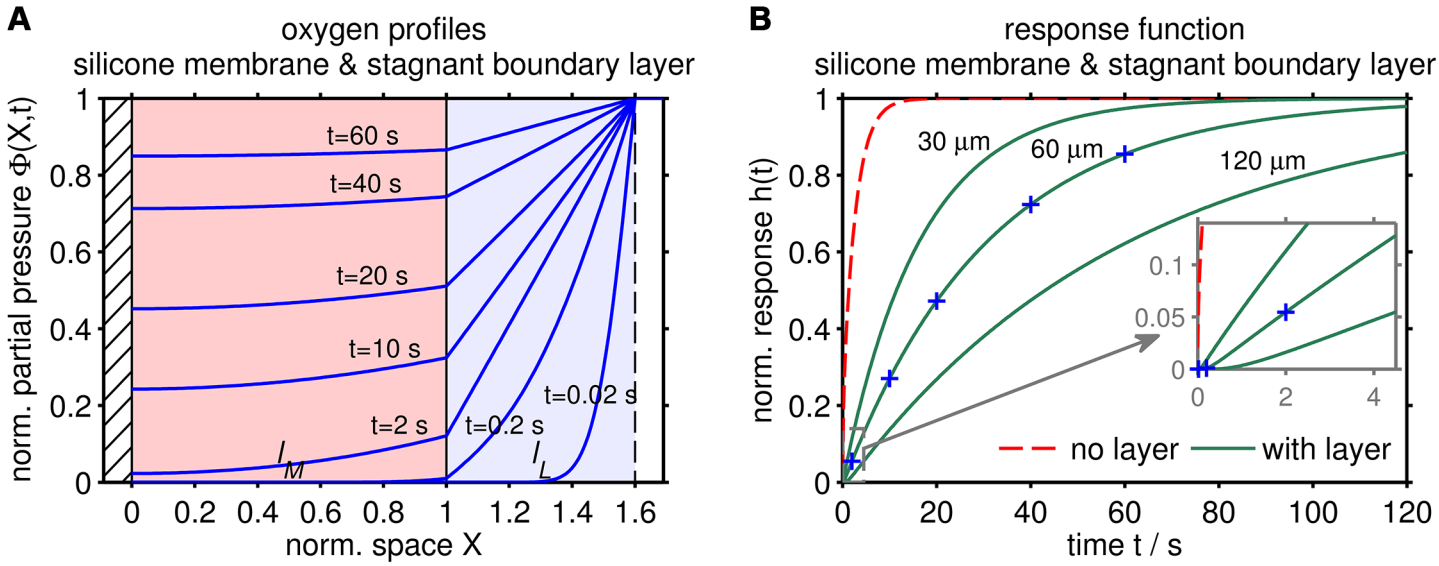


**Fig. 1.** Two-layer diffusional optode model consisting of a silicone membrane ($0 \le X \le 1$, $l_M$ = 100 µm, Aanderaa optode standard foil) with impermeable boundary (hatched, optical window) on one side and a stagnant boundary layer ($1 \le X \le (l_M + l_L)/l_M$, $l_L$ = 60 µm, slow CTD cast) on the other side ($T$ = 25°C). (a) Oxygen profiles inside the two layers after an ambient step change in normalized partial pressure $\Phi(X > (l_M + l_L)/l_M, t = 0)$ from 0 to 1. $O_2$ only reaches the membrane after permeating the boundary layer, and the $O_2$ supply is limited by the $O_2$ diffusion along the boundary layer gradient. (b) Step response function $h(t)$ for different boundary layer thicknesses $l_L$ (green) and for a gas phase time response ($l_L$ = 0 µm, dashed red).

**Table 2.** Summary of both flow speed ($s$) and temperature ($T$) laboratory and field experiments with associated sensor serial numbers if the sensor model was present.

| | | | Sensor model/serial number | | | | |
|---|---|---|---|---|---|---|---|
| **Exp. nr** | **Experiment type** | **Experiment label** | **3830** | **4330** | **4330F** | **SBE63** | **Rinko** |
| 1 | lab ($s$) | flow speed | | 1225 | 135 | 392 | |
| 2 | lab ($T$) | pumped | | 1225 | 135 | 115 | |
| 3 | lab ($T$) | lab standard | 1260 | 183 | 207 | | |
| 4 | lab ($T$) | "slow-platform" | | 845 | 207 | 115* | 54 |
| 5 | field | ANT-XXVII/2 | 529 | | 207 | | 10 |
| 6 | field | MSM 18/3 | | 564 | | | |
| 7 | field | glider | 1059 | | | | |
| 8 | field | polar floats | 8 units | | | | |
| 9 | field | $CO_2$ float | 1 unit | | | | |

*The SBE63 was used unpumped with bare optical window for experiment 4.

sional model can be found in the appendix.

**Laboratory experiments**

Laboratory experiments were designed as isothermal step response experiments. An aquarium pump and a $N_2$ gas cylinder were used to adjust the oxygen content of two water reservoirs, one close to air saturation and one strongly depleted in $O_2$. These two reservoirs were at the same temperature and the sensors were switched between them (ca. 10 times in both directions). With this design, both falling (air → $N_2$) and rising ($N_2$ → air) steps can be observed.

To investigate the flow speed and temperature influence on the sensor's time response separately, two types of laboratory experiments were done: One where the flow rate was varied while the temperature was kept constant at 25°C (experiment 1), and three where the mixing was kept constant while data were obtained at different temperatures (experiments 2–4). Table 2 gives a summary of both the laboratory and field experiments (explained below), and the sensors used for each setup.

For the flow speed experiment 1, a pumped setup was used in combination with the SBE63's plenum or a custom flow cell for the Aanderaa optodes, and a three-way valve to switch the two reservoirs. The flow rate was adjusted using an Ismatec Ecoline VC-380 peristaltic pump (Ismatec GmbH, Wertheim/Germany) (100–2500 mL $min^{-1}$) or a SBE 5P/5T pump (7000 mL $min^{-1}$), respectively. The manufacturer's

plenum for the SBE63 has a small inner volume of 3.5 mL, whereas our plenum for the Aanderaa optodes has 23.5 mL.

For the temperature experiments, three different flow regimes were chosen. For the pumped experiment 2, the same setup as above was used with the highest flow rate but the temperature of the reservoirs and sensors varied between 2°C and 32°C. Experiment 3 resembled the most common laboratory setup to determine response times (Tengberg et al. 2006; Uchida 2010), using two thoroughly stirred beakers as reservoirs and moving the sensors quickly between both. Finally, experiment 4 imitated slowly moving platforms such as gliders and floats. As gently stirred reservoirs, the internal bowls of two identical cryostats (F25, Julabo GmbH, Seelbach, Germany) were used. Again, sensors were switched by moving them quickly between both reservoirs. For this experiment, the plenum of the SBE63 was removed, and all sensors used with bare optical windows. It needs to be stressed that using the SBE63 unpumped is not intended by the manufacturer.

For quantification, all step response curves $h(t)$ were fitted individually and outliers detected and removed using a generalized extreme Studentized deviate (ESD) test (Rosner 1983). Fig. 2 shows an example of the (normalized) step response curves for optode 3830 SN 1260 at 16°C during experiment 3. The fit equation for the exponential response time τ is given in Eq. 3

$$h(t) = A \cdot \left(1 - e^{-\frac{t-t_0}{\tau}}\right) \quad (3)$$

where $A$ is an amplitude to match the height of the step and $t_0$ is a time offset to precisely match the start of the step within the time-discrete sensor samples. The boundary layer thickness $l_L$ was obtained analogously from the step response curves $h(t)$. Because the results from rising and falling steps are indistinguishable (*see* Fig. 2), they are merged for clarity in all subsequent plots.

**Field experiments**

The field experiments feature the major profiling platforms commonly equipped with oxygen sensors. Hydrocasts with a CTD (experiments 5 and 6) and profiles by autonomous gliders and floats (experiments 7–9).

Table 3 gives a summary of the technical data for the field deployments, i.e., the number of profiles for each sensor, the duration of the acquired record together with the sampling rate as well as the velocity and temperature regime of the deployment. The sensors used in each experiment are given in Table 2.

In these field applications, the optode essentially measures a delayed, filtered version of the true oxygen profile.

The in situ model below (Eqs. 4–6) mimics the optode by applying a single-pole low-pass filter on the "true" oxygen profile, i.e., by convoluting the optode time response with the "true" oxygen profile. Its purpose is to obtain an in situ response time τ. The "true," in situ oxygen profile originates from a fast responding reference sensor (e.g., a SBE43 clark-type electrode, Eq. 6) on the same platform or from a co-located reference profile through an isopycnal match. The bilinear $Z$-transform (Eq. 4, *see* "Appendix") of the time-continuous response (Eq. 3) is used for the time-discrete data.

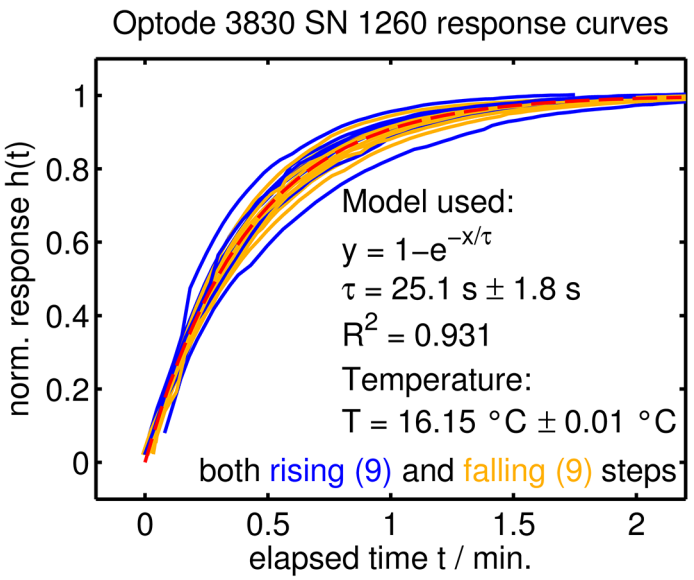


**Fig. 2.** Normalized step response curves $h(t)$ for optode 3830 SN 1260 at 16°C (experiment 3) with exponential fit (red dashed line).

**Table 3.** Specifications of the CTD, glider, and float field experiments.

| Exp. nr | Experiment label | Sensor model | Nr of profiles | Duration of profiles | Sample interval | Vel. range/ dbar $s^{-1}$ | T range/ °C |
|---|---|---|---|---|---|---|---|
| 5 | ANT-XXVII/2 | 3830 | 149 | 322 h | 5 s | 0.5 – 1.2 | –1.1 – 2.5 |
| 5 | ANT-XXVII/2 | 4330F | 175 | 324 h | 5 s | 0.5 – 1.2 | –1.1 – 2.5 |
| 5 | ANT-XXVII/2 | Rinko | 168 | 332 h | 24 Hz | 0.5 – 1.2 | –1.1 – 2.5 |
| 6 | MSM 18/3 | 4330 | 13 | 11 h | 5 s | 0.2 – 1.0 | 4.7 – 26.4 |
| 7 | glider | 3830 | 65 | 108 h | 2 s | ca. 0.3 | 5.6 – 28.5 |
| 8 | polar floats | 3830 | 8 | 52 h | 50 – 600 s | 0.09 | –1.4 – 3.9 |
| 9 | $CO_2$ float | 3835 | 1 | 2 h | ca. 150 s | 0.03 | 14.1 – 27.1 |

$$c_{i+1}^{\text{filt}} = a \cdot c_i^{\text{filt}} + b \cdot \left( c_{i+1}^{\text{in situ}} + c_i^{\text{in situ}} \right),$$
$$a = 1 - 2b, \qquad b = \left( 1 + 2\frac{\tau}{t_{i+1} - t_i} \right)^{-1} \tag{4}$$

$$c_{i=0}^{\text{in situ}} - c_{i=0}^{\text{filt}} = f_0 \tag{5}$$

$$c_i^{\text{in situ}} = c_i^{\text{SBE43}} + r \tag{6}$$

The filter was applied to a short interval of the "true" in situ oxygen profile $c^{\text{in situ}}$ following the recursive Eq. 4 with the initial condition Eq. 5 and the calibration offset $r$ (Eq. 6). The latter allows to compensate for a possible calibration mismatch between optode and SBE43 that would otherwise bias the model fit.

Fig. 3 illustrates the in situ model, which foremost approximates the shape of the profile. In the example, the quasi-continuous SBE43 record $c^{\text{SBE43}}$ provides the reference $O_2$ profile shape. Within a short time window, the profile data are filtered with a response time $\tau$ to simulate the effect of the optode response ($c^{\text{filt}}$). The response time $\tau$ is then iteratively refined (as well as $f_0$ and $r$) until the filtered profile $c^{\text{filt}}$ matches the discrete optode record $c^{\text{optode}}$.

By letting the time window float through the entire profile record, an in situ response time $\tau$ is thus obtained for each optode observation. Strictly speaking, it is rather a response time difference to the reference sensor, but the standard processing (e.g., for the SBE43, see Edwards et al. 2010) is assumed to produce a reference profile with zero lag. Due to the short duration of the time window, changes in velocity $s$ and temperature $T$ were small (90th percentile of $\sigma(s)$ and $\sigma(T)$ at 0.2 dbar $s^{-1}$ and 0.5°C for 6) and therefore, a mean value was used to characterize each time window.

The response times follow an inverse Gaussian distribution. Therefore, all plots of field data in the "Assessment" section show only the respective distribution's mode (i.e., most frequent) value, the distribution's width, and its mean value. Further technical and quality control aspects of this approach are detailed in the appendix.

## *Assessment*

The assessment starts with the laboratory experiments 1–4, i.e., the flow speed and temperature dependence of the time response. It continues with a discussion of the CTD field deployments (5 & 6). Subsequently, the time response impact on data and a possible reconstruction of an original $O_2$ profile are illustrated with these data. At the end, the assessment proceeds with the glider and float field deployments (7–9).

**Flow speed dependence**

All sensors show the same behaviour: both the response time $\tau$ and the boundary layer thickness $l_L$ are inversely proportional to the flow speed (Fig. 4). However, the sensors are

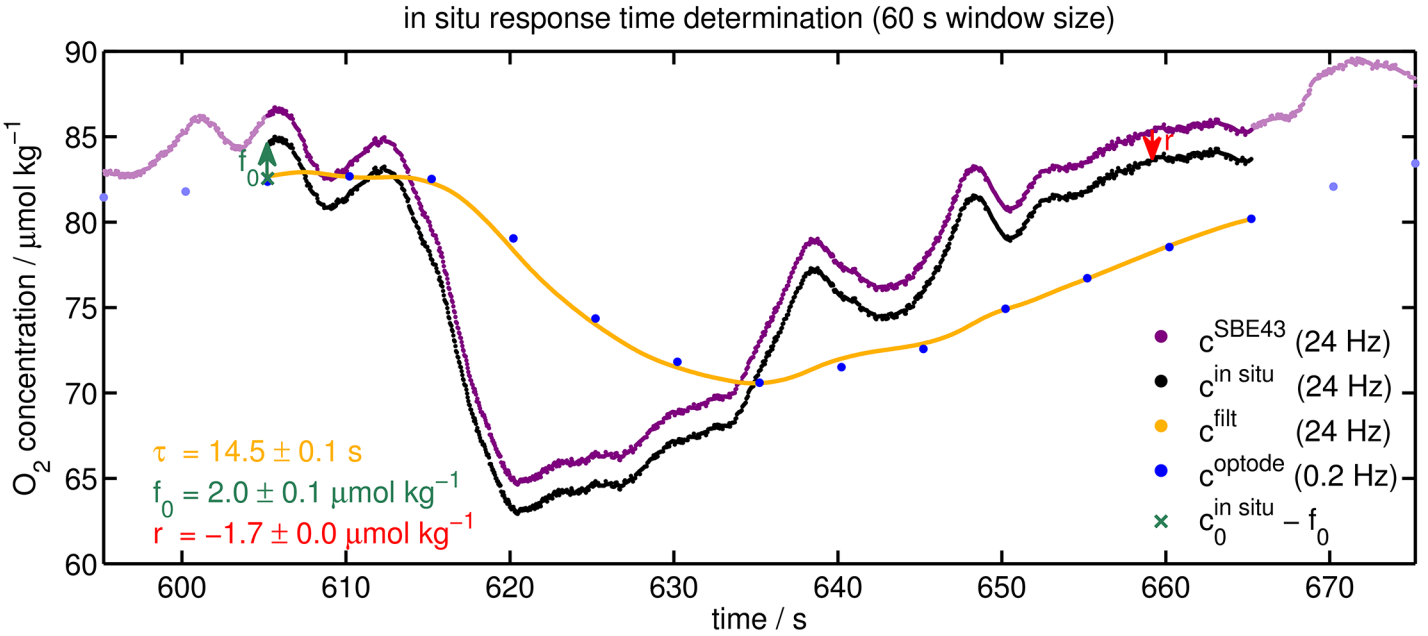


**Fig. 3.** Illustration of the in situ model. The optode observations (blue dots) are approximated within a 60 s time window (i.e., 605–665 s of the cast) by $c^{\text{filt}}$ (yellow dots), which is the in situ $O_2$ (black dots) filtered with the time constant $\tau$. The in situ $O_2$ is based on the SBE43 observations (purple dots) allowing for a calibration offset $r$ (red arrow) within the fit routine. The initial forcing $f_0$ (green arrow) defines the start member (green cross) of the filter. The parameters and initial condition are given with their 95% confidence bounds. (During this 60 s time window, the temperature was 9.0 ± 0.4°C and the CTD descended from 394 dbar to 456 dbar.)

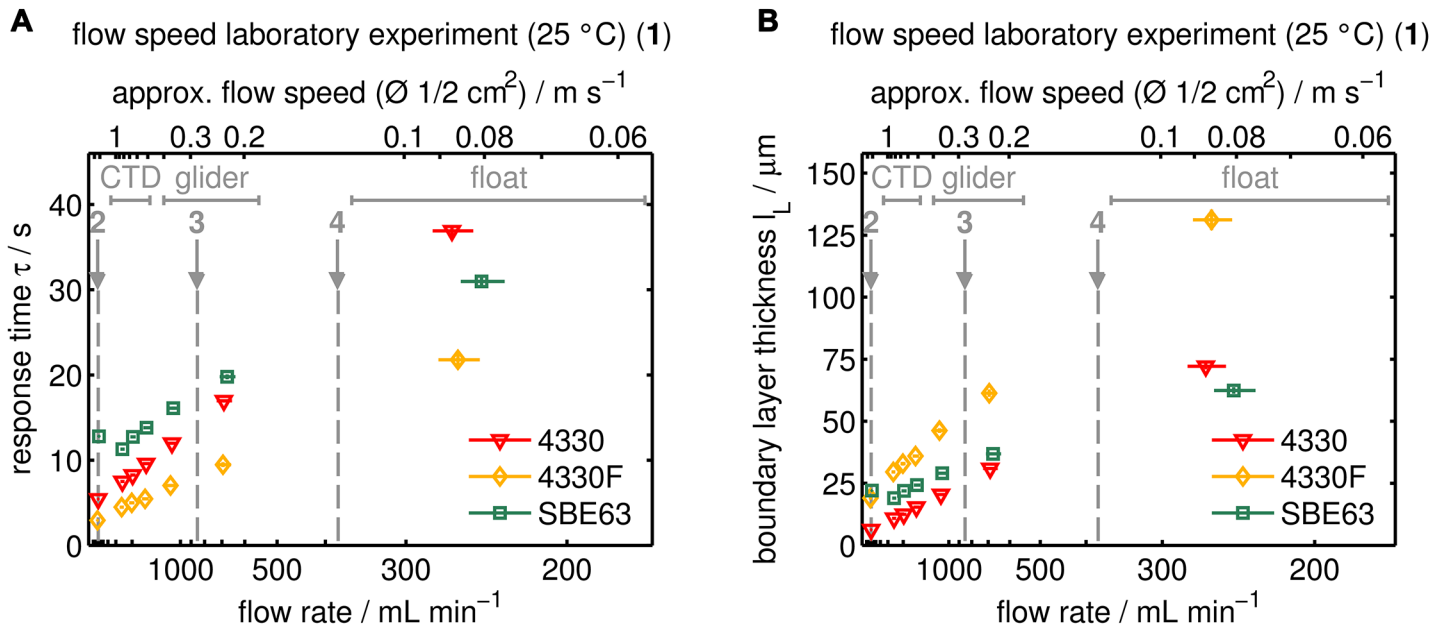


**Fig. 4.** Flow rate dependence of the time response at 25°C (experiment 1). Data are plotted versus the reciprocal flow rate for both methods, the exponential approach (a) and the two-layer diffusional model (b). Flow rates were converted to an estimate of the flow speed using a plenum cross section of 1/2 cm². Gray arrows denote approximate flow regimes used for the temperature dependent experiments 2–4 (Fig. 5). Approximate regimes for field platforms are indicated by gray bars.

not fully comparable since the geometry of the custom Aanderaa optode's flow cell and the SBE63 plenum differed somewhat. The flow hit the optical window of the Aanderaa optodes in a 45° angle while it passed it tangentially in the SBE63 plenum. Moreover, the dead volume of the plenums were different (23.5 mL versus 3.5 mL), affecting the mixing time inside the plenum. The data presented here are not corrected for any such geometry effect.

Given the large spread of flow rates during experiment 1, response times τ vary between a few seconds and close to a hundred seconds at 100 mL min$^{-1}$ (data not shown). Compared with that, differences between sensors are small, e.g., an Aanderaa optode model 4330 with standard foil can achieve the same response time as a model 4330F with fast response foil if the flow rate is doubled. At the same time, all sensors can yield response times τ below 10 s if they are used in pumped mode (experiment 2).

For the diffusional model (Fig. 4b), a sensing membrane thickness $l_M$ of 100 µm was used for the Aanderaa standard foil (model 4330), whereas 30 µm was used for the fast response foil (model 4330F) (PSt3 membranes, Huber 2010). The SeaBird SBE63 optode was treated in the same way as the PSt3 standard foil.

When extrapolated to infinite flow rates, the boundary layer should vanish completely ($l_L^\infty \rightarrow 0$ µm) and only the sensing foil time response should remain. This is indeed found for the standard foil model 4330 ($l_L^\infty = 4 \pm 4$ µm, ± 1σ). The fast response model 4330F and the SBE63 optode, however, have a significant non-zero intercept ($l_L^\infty = 18 \pm 4$ µm and $l_L^\infty = 14 \pm 3$ µm, respectively). This indicates that part of the sensing membrane time response gets falsely attributed to the boundary layer.

To obtain consistency within the diffusional model, $l_M$ was adjusted to 50 µm for the fast response foil and to 130 µm for the SBE63 optode hereafter. In fact, all three sensors then follow the same $l_L$ – flow rate dependence (not shown), indicating that the diffusional model is suitable to characterize the boundary layer processes in front of the sensor membrane for all sensors.

Based on boundary layer theory (Schlichting and Gersten 1997), the thickness of the velocity boundary layer is inversely proportional to the square-root of the Reynolds number and thus flow speed. $l_L$ scales accordingly which leads to the faster response at high flow rates.

**Temperature dependence**

From the spread of flow rates of experiment 1, three distinct regimes were chosen to analyze the temperature influence: experiment 2 with pumped sensors at the high end (Fig.!5a and 5b), experiment 3 with thoroughly stirred beakers (Fig. 5c and 5d) to provide results comparable with other lab studies, and experiment 4 at the low end (Fig. 5e and 5f) to imitate comparatively slow, buoyancy-driven platforms such as floats and gliders.

At low temperatures, solubilities $S(T)$ increase so that more $O_2$ molecules have to diffuse into the sensing membrane to obtain the same $pO_2$, i.e., the same response. At the same time, diffusivities $D(T)$ decrease so that this diffusion takes longer.

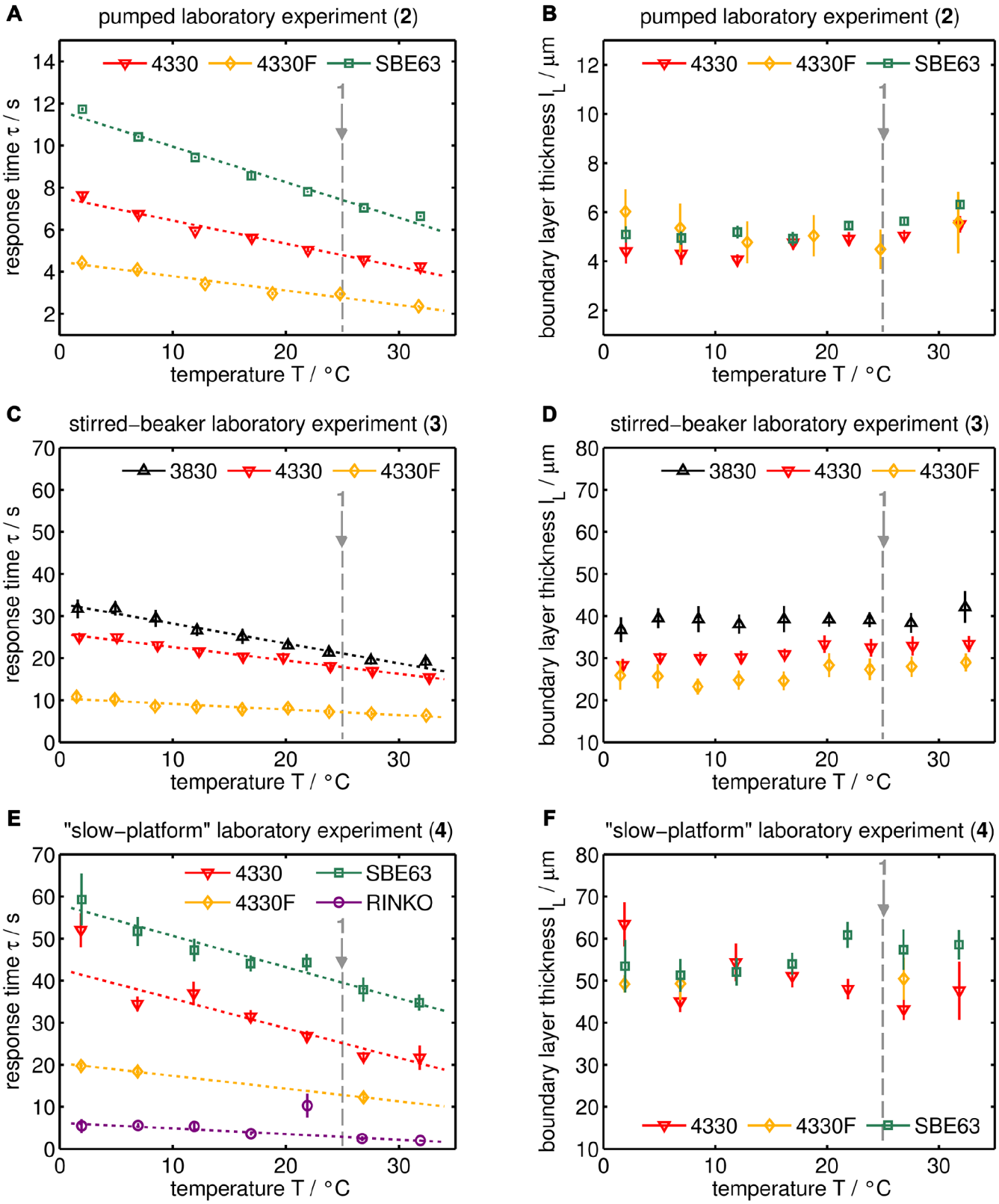


**Fig. 5.** Temperature dependence of the time response at three flow regimes. Experiments (from top to bottom) are a pumped setup 2 (a and b), a stirred-beaker standard setup 3 (c and d), and a "slow-platform"-imitating setup 4 (e and f). Results are shown for both an exponential approach (left column) and a two-layer diffusional model (right column). The gray arrow denotes the temperature of the flow speed experiment 1 (Fig. 4).

Both effects lead to markedly increased response times $\tau$ at low temperatures. Over the temperature range 2°C–34°C, response times $\tau$ vary by approximately ± 25% around the mean value.

The boundary layer thickness $l_L$, however, is rather constant for a given experiment, indicating that molecular diffusion is the dominant process for the temperature dependence.

Experiment 2 yields a number of useful results: (a) The sensor time response can be accelerated when used in a pumped setup, an approach that has been realized for the SBE63. (b) A pumped setup yields a highly reproducible time response (95% confidence intervals are hardly visible in Fig. 5a). (c) With a boundary layer of only ca. 5 μm, response times $\tau$ in experiment 2 are close to their lower limits (i.e., the gas phase response).

The SBE63 optode appears to use a thicker sensing foil than the Aanderaa standard foil model 4330, or the geometry effect of the plenum is of considerable importance (see also experiment 1).

In a pumped setup, sensors can be even faster than claimed by the manufacturer, see, e.g., the Aanderaa optode specifications in Table 1. Moreover, boundary layer thicknesses $l_L$ vary only marginally (4 μm–6 μm), show no temperature dependence, and are the same for all sensors.

The standard laboratory time response setup with stirred beakers (experiment 3) gives results similar to the ones reported in the literature (see Table 1, Aanderaa Data Instruments AS 2012, and Tengberg et al. 2006), with response times $\tau$ for the standard foil models 3830 and 4330 around 25 s and around 8 s for the fast response foil model 4330F. Again, the boundary layer thickness for both the 4330 and the 4330F optode are comparable ($l_L \approx 29 \pm 5$ μm), supporting the validity of the diffusional model. The somewhat higher values for the 3830 optode might be an effect of the different geometry of that model compared to the 4330 optode.

Finally, experiment 4 imitates the least-turbulent deployment platforms and provides the following findings: (a) The Aanderaa optode model 4330 appears to use a slightly thinner membrane than the SBE63 optode and is therefore, in principle, faster. (b) The JFE Alec Co. Rinko sensor is the fastest of all optodes, although its response time $\tau$ is an order of magnitude higher than claimed by the manufacturer (see Table 1, JFE Alec Co. 2009). (c) Even with slow response times $\tau$, their temperature dependence is explained by solubility $S(T)$ and diffusivity $D(T)$ variations (i.e., $l_L(T)$ is approximately constant).

No sensing membrane thickness $l_M$ was available for the JFE Alec Co. Rinko. If it were zero, the liquid boundary layer $l_L$ would have to be around 133 ± 32 μm for the observed time response (Fig. 5e). This is unrealistically high compared with the other three sensors of experiment 4 (Fig. 5f). Rather, the sensor's coating itself possesses a response delay (i.e., it needs to be "filled" with $O_2$), which is falsely attributed to the boundary layer.

**CTD field experiments**

CTD-mounted optodes were investigated on two cruises: the R/V *Polarstern* cruise ANT-XXVII/2 (Rohardt et al. 2011) to the Southern Ocean (experiment 5) and the R/V *Maria S. Merian* cruise MSM 18/3 (Krahmann and Fischer 2012) to the Eastern Tropical North Atlantic (experiment 6). On both cruises, a calibrated SBE43 sensor served as reference to derive the optode's in situ response times $\tau$. The results of both experiments are presented in Fig. 6. The left panels show photographs of the sensors' attachments to the CTD frame, whereas the middle and right panels show the binned in situ response time distributions versus vertical velocity and temperature, respectively.

The flow speed was the dominant factor in the laboratory experiments 1–4. In fact, a flow speed dependence can be seen with the field data of the JFE Alec Co. Rinko in experiment 5 (Fig. 6b) and much more obvious with the Aanderaa optode in experiment 6 (Fig. 6c). In both settings, the optical window pointed downward and the sensors were attached without obstacles to the flow nearby. The optodes' time response is fastest during downcast and slowest when the CTD was near-stationary or hoisted slowly, with a factor of 2 in between the bins' response times $\tau$.

In contrast, the Aanderaa optodes in experiment 5, attached in horizontal direction close to a bar of the CTD frame, show no sign of a speed dependence (Fig. 6a). In fact, the frame seems to create a regime of constant local turbulence, even at low speeds.

The mode of attachment and orientation of a sensor is therefore a crucial part of the setup design.

Both experiments 5 and 6 support the temperature dependence found in the laboratory (experiments 2–4), being slower at low temperatures (Fig. 6, right panels). Still, the spread of the field data (and the limited temperature range of 5) would have made it difficult to derive a temperature relation without the laboratory evidence.

The average response times $\tau$ of 35 ± 15 s and 14 ± 10 s for the Aanderaa optodes model 3830 and model 4330F in 5 translate to a boundary layer thickness $l_L$ of 41 ± 21 μm for the standard foil and 39 ± 32 μm for the fast response foil (±1 σ). Regarding the Rinko sensor, the field analysis yields an average response time of 4.7 ± 2.6 s, compared with the processed SBE43 reference (Edwards et al. 2010). This appears to be a more suitable estimate of the Rinko response time $\tau$ under real conditions than the gas phase response time given by the manufacturer (Table 1).

For the standard foil model 4330 in 6, however, the $l_L$ varies between 19 ± 4 μm when the sensing foil is hit directly (+1.0 dbar $s^{-1}$ bin) and 48 ± 18 μm when it is effectively shaded by the CTD body and Niskin bottles (0.0 dbar $s^{-1}$ & –0.5 dbar $s^{-1}$ bins).

**Time response impact and oxygen data reconstruction**

The effect of the time response on data acquired in the field is discussed below. As an example, a CTD station from experiment 6 at 4.5° N 23° W located in the oxygen minimum zone off Northwest Africa is used. Besides substantial $O_2$ gradients throughout the profile, both temperature and vertical velocity vary during this CTD cast, so their combined effect can be illustrated.

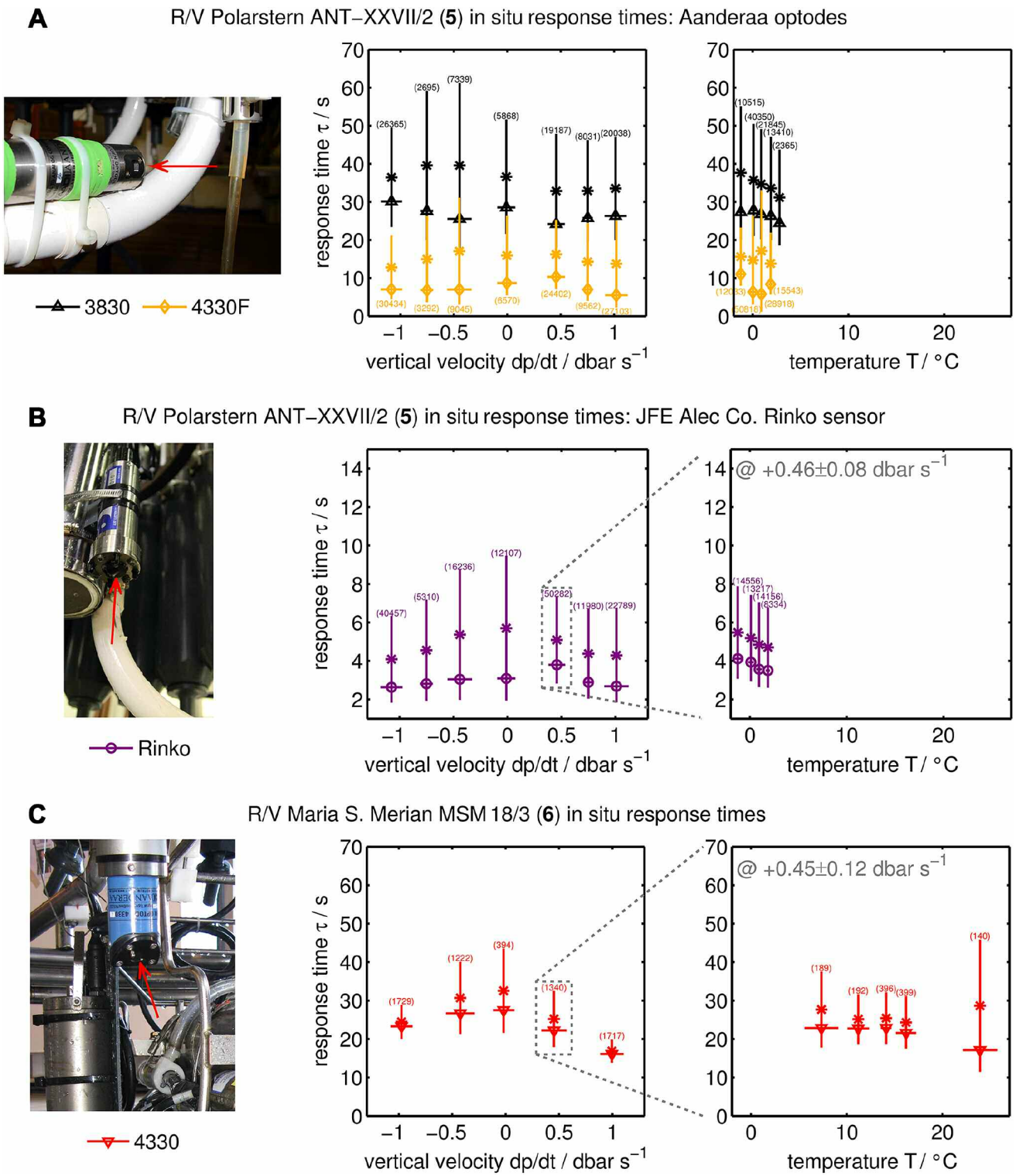


**Fig. 6.** In situ response times for CTD experiments 5 and 6. Left panels: Sensor attachment and orientation at the CTD frame. The red arrow points at the optical window. During R/V *Polarstern* ANT-XXVII/2 (5), both Aanderaa optodes were attached adjacent to a horizontal bar with the optical window facing out horizontally (a). In contrast, the JFE Alec Co. Rinko sensor (5) (b) and the optode during R/V *Maria S. Merian* MSM 18/3 (6) (c) were attached without obstacles nearby and with the optical window facing downward. Middle panels: In situ response time $\tau$ against CTD vertical velocity with mode value (marker), distribution width (bar, mean $\pm$ $\sigma$), and mean value (asterisk). The number of observations in each bin is given in parentheses. Right panels: In situ response time $\tau$ against temperature. For the JFE Alec Co. Rinko data of 5 and for 6, only one distinct velocity bin (grey dotted box) was used due to the flow speed dependence.

For a given $O_2$ profile, the optode measures a filtered analogue (see Eq. 4). This filter has two effects: (a) Fine scale structure of the original $O_2$ profile is lost. (b) The sensor responds with a delay to every gradient.

The effects are cumulative, i.e., a gradient or forcing a moment ago still has an influence on the current measurement. So every past fluctuation or gradient (weighted with the scale of the response time) has, in principle, an influence on the measurement error $\beta_i^{\text{filt}}$ between true profile $c_i^{\text{in situ}}$ and filtered measurement $c_i^{\text{filt}}$.

$$\beta_i^{\text{filt}} = c_i^{\text{filt}} - c_i^{\text{in situ}} \tag{7}$$

However, since the fine scale structure shows both positive and negative fluctuations, these tend to cancel out. In contrast, water mass gradients tend to persist longer than the timescale of the time response. They are in fact the main cause for the observed measurement error β.

The error β depends on the local forcing δ, defined as

$$\delta = -g \cdot s \cdot \tau(T) = -\frac{dc}{dp} \cdot \frac{dp}{dt} \cdot \tau(T) \tag{8}$$

with $g = dc/dp$ being the $O_2$ gradient and $s = dp/dt$ the vertical velocity. β is essentially the filtered version of δ.

Fig. 7 shows both the downcast and upcast of the above-mentioned CTD station, with the $O_2$ profile on the left and the measurement error β on the right. Apart from the reference profile (black) and the optode measurements (blue), it contains a simulation of the optode time response (yellow) based on the reference and a reconstruction of the original profile (red) based on the optode (details below).

The fine scale fluctuations of the reference profile (black) between 500 dbar and 600 dbar are not grasped by the optode measurements (blue), but do not cause a strong error either. The surface oxycline around 100 dbar, however, causes a significant error because it represents a strong peak in the local forcing δ due to its extreme gradient. For the upcast, the measurement error β then declines exponentially as there are no

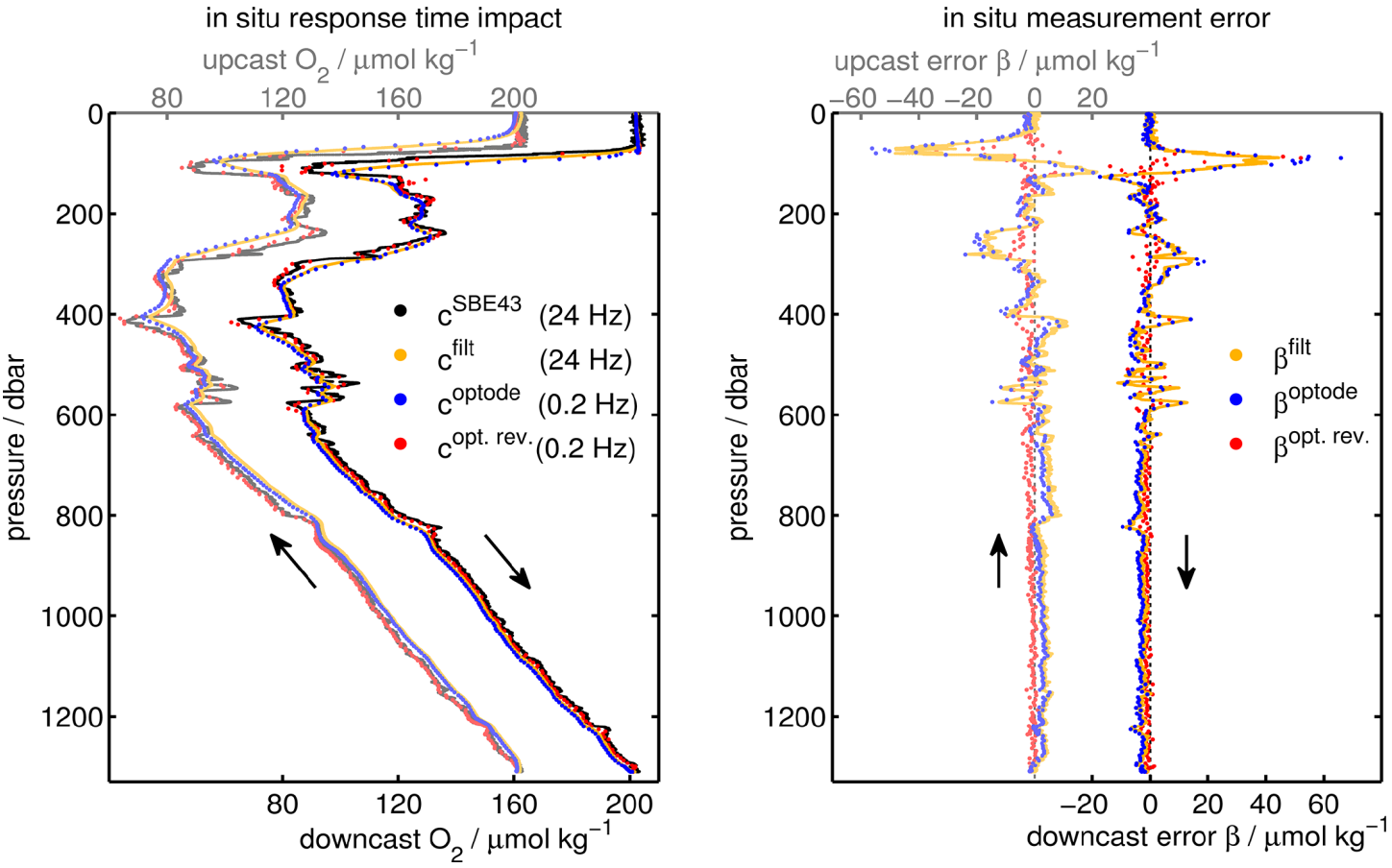


**Fig. 7.** Downcast and upcast (brighter coloured and offset by –40 µmol kg$^{-1}$) $O_2$ profile (left) and measurement error β (right) as acquired at the R/V *Maria S. Merian* MSM 18/3 CTD station at 4.5° N 23° W (experiment 6). The quasicontinuous and fast SBE43 reference data are given in black. The simulated optode-like time response is shown in yellow and the actual optode observations (model 4330) are given in blue. The different contributions to the measurement error are illustrated in Fig. 8. The red dots show the reconstruction of the original $O_2$ profile from the optode observations.

further gradients (i.e., $\delta = 0$) in the surface mixed layer.

The different factors affecting the optode time response are separated in Fig.!8 for the downcast section of the same profile.

The low velocities in the upper 200 dbar cause a thicker boundary layer than for the remainder of the downcast, but high surface temperatures lead to relatively small response times. At greater depths, high velocities lead to a considerably thinner boundary layer but low temperatures increase response times. The resulting response time $\tau$ is therefore only 5–10 s higher in the surface than at depth. Still, gradients are highest near the surface, and thus, is the local forcing $\delta$ as well as the (accumulated) measurement error $\beta$.

For the simulation of the optode time response (yellow in both Figs. 7 and 8), response times $\tau$ were derived using the boundary layer $l_L$ – vertical velocity $s$ relation from experiment 6 and then converting $l_L$ to response times $\tau$ at in situ temperatures.

The reverse operation to simulating the optode time response, i.e., the reconstruction (or deconvolution) of the original profile from time-lagged measurements, is of great importance for practical applications. However, this approach has some major caveats: (a) The reconstruction or deconvolution severely amplifies noise in the data. (b) The data sample interval should be about an order of magnitude shorter than the response time.

Dedicated algorithms have been developed for the noise issue to minimize processing artefacts (e.g., Miloshevich et al. 2004). These have been applied both to atmospheric data (e.g., radiosonde humidity measurements, Miloshevich et al. 2004) and oceanic data (e.g., float $pCO_2$ measurements, Fiedler et al. 2013) and are used in this work as well (*see* "Appendix").

The reconstruction is shown in red in Fig. 7. Despite the fact that the sample interval condition given above is poorly met (5 s sample interval versus ca. 20 s response time), the deconvolution still gives a reasonable result (root-mean-square error of 4.8 μmol kg$^{-1}$ compared to 9.7 μmol kg$^{-1}$ for the original sensor data). Moreover, realistic finescale features are restored but artefacts occur at strong gradients, e.g., the subsurface oxycline. A higher temporal resolution might have improved the reconstruction in these parts of the profile.

**Glider field experiment**

A Slocum glider (Teledyne Webb Research) was used for experiment 7 with an Aanderaa optode model 3830 attached

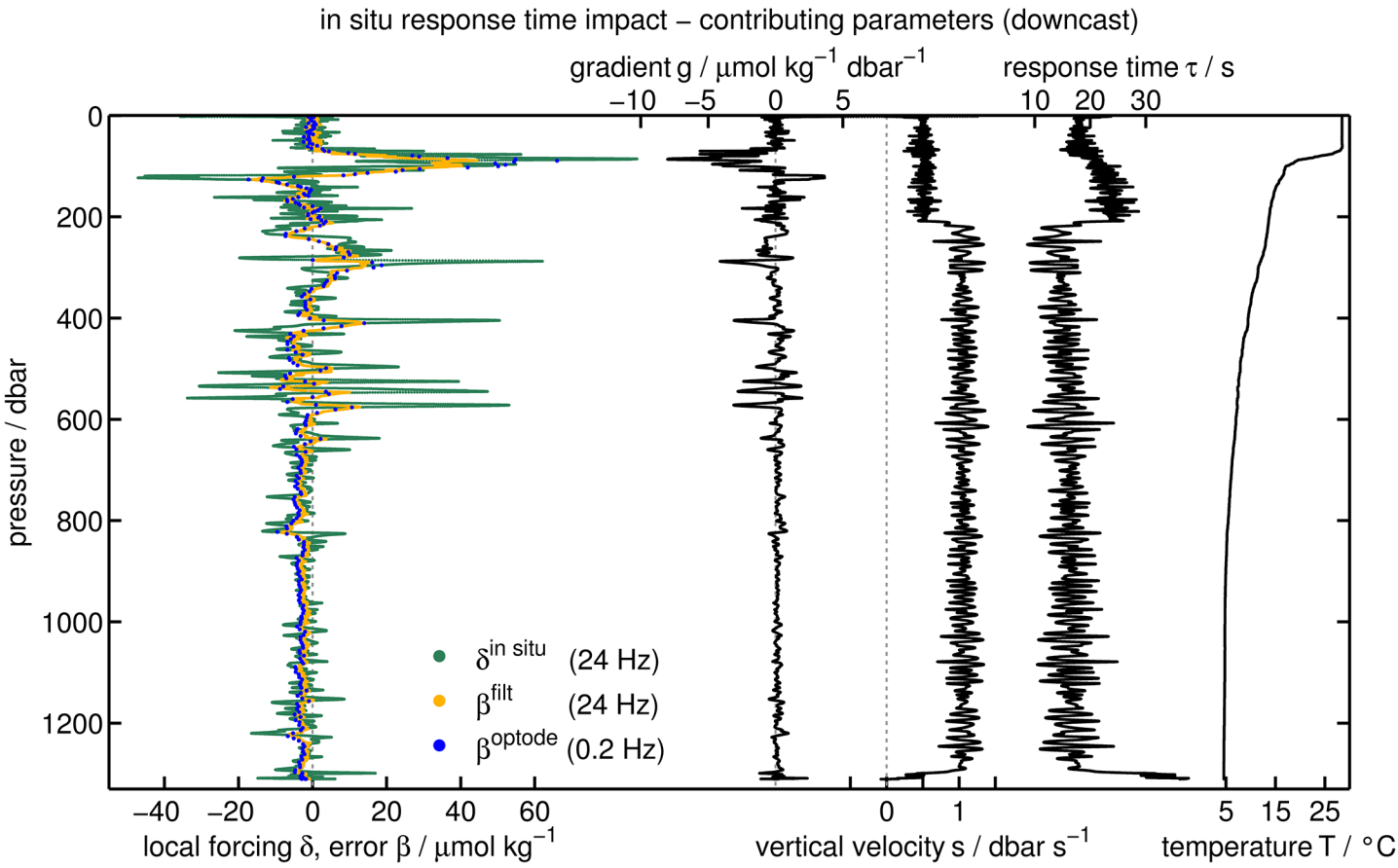


**Fig. 8.** Modeled and observed measurement error $\beta$ and its influence factors for the downcast at R/V *Maria S. Merian* MSM 18/3 CTD station at 4.5° N 23° W (experiment 6). The local forcing $\delta$ is the product of $O_2$ gradient $g$, vertical velocity $s$, and response time $\tau$. Applying the filter to the local forcing $\delta$ directly gives the measurement error $\beta$. The temperature effect on the response time $\tau$ is pronounced near the surface where velocities are small.

close to the glider's tail. It was deployed during R/V *Maria S. Merian* cruise MSM 22 near 5° N 23° W and circled around a mooring at that location. The glider cycled the upper 900 m of the water column, regularly crossing the thermocline. For comparison, a total of 6 CTD casts were performed during the glider's 3-week deployment period within a distance of 10 nm. Only glider dives with a time difference below 8 hours were considered, and results are given in Fig.!9.

The glider's speed was derived from the vertical velocity, the pitch angle, and an assumed angle of attack of 3°. It is relatively constant for this buoyancy-driven platform. However, the upcasts in experiment 7 are slightly faster as are the upcast response times τ, reflecting the flow speed influence. More dominantly, however, a strong temperature effect can be seen in the response times τ for both the downcast (middle panel) and the upcast (right panel). The diffusional model is able to explain the temperature dependence of the mode value of the response time distribution. However, there is a significant fraction of very high response times τ, which considerably broaden the width of the distribution.

Given the broad and asymmetric distribution, a mean response time τ seems of little value. Translated to a boundary layer thickness $l_L$, the downcast ranges at an average of 110 ± 86 μm whereas the upcast yields 71 ± 60 μm (± 1σ).

**Argo-float field experiments**

For the polar float experiment 8, a total of 8 floats (each with an Aanderaa optode model 3830) were deployed in polar seas: 6 during R/V *Polarstern* cruise ANT-XXVII/2 (see experiment 5) in the Weddell Sea and 2 during R/V *Oceania* cruise AREX10 along 75° N in the West Spitsbergen Current. The floats had a typical ascent velocity of –0.087 ± 0.002 dbar $s^{-1}$, and they did log the time stamp for each float observation. This allowed the comparison to CTD profiles measured nearby.

For the cold waters, the floats gave response times τ around 190 ± 230 s and an average $l_L$ of 210 ± 230 μm, much larger than anticipated from the laboratory experiments alone. However, their results are badly constrained as they measured their first profile only 10 days after deployment, which adversely affects the match between float and CTD-based reference profile.

A slightly different float was used for the $CO_2$ float experiment 9. It was equipped with an Aanderaa optode model 3835, a shallow water version of the model 3830, and a $pCO_2$ sensor (see Fiedler et al. 2013). The float was deployed in the vicinity of the Cape Verde Ocean Observatory (CVOO, 17.6° N 24.3° W, http://cvoo.geomar.de), located in the Eastern Tropical North Atlantic oxygen minimum zone. In contrast to standard Argo floats, it performed a test profile just after its deployment. This allowed a more direct comparison to a CTD profile measured by R/V *Islândia* directly after completion of the first profile on-site. Both profiles are shown in Fig.!10, together with a simulation of the optode time response.

A boundary layer thickness $l_L$ around 440 ± 80 μm was found to match the observations of experiment 9 best. This equals response times τ around 280 ± 50 s, even higher than for the polar floats (experiment 8) despite the warmer temperatures. However, this experimental float showed an average ascent speed of only –0.026 ± 0.012 dbar $s^{-1}$ for the 200 m profile, which is very slow even for a float. The extremely low velocity environment thus causes the high response times.

Still, even with such high response times τ, the measurement error during experiment 9 is as low as 4 μmol $kg^{-1}$ on average and does not exceed a maximum of 16 μmol $kg^{-1}$. This is due to the float's slow progression through the water col-

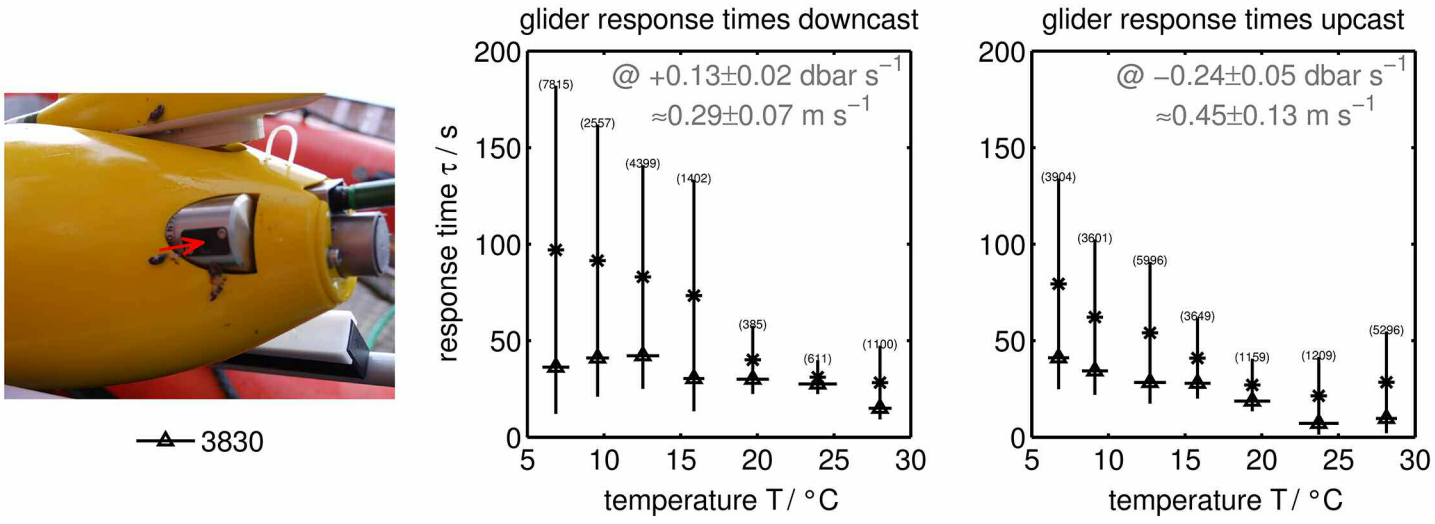


**Fig. 9.** Results of the field deployment on a Slocum glider during R/V *Maria S. Merian* MSM 22 (7). Left panel: Sensor attachment and orientation of the optode at the glider's tail. The red arrow points at the optical window. Middle and right panel: In situ response time distribution for the downward and upward dives against temperature with mode value (marker), distribution width (bar, mean ± σ), and mean value (asterisk). The number of observations per bin is given in parentheses.

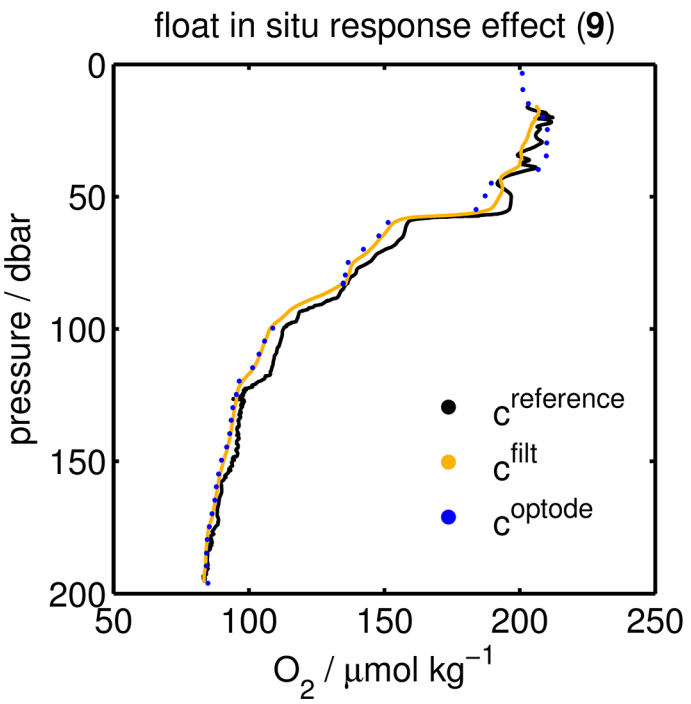


**Fig. 10.** Oxygen profile of an experimental Argo-$O_2$/$pCO_2$ float (blue) with co-located reference profile from R/V *Islândia* (black) and simulated sensor time response (yellow) (experiment 9).

umn including gradient regions, which counterbalances the high response times τ (see Eq. 8).

## Summary

Oxygen optode response times τ vary over a large range depending on the flow speed and temperature regime of the application. They can be as short as a few seconds in pumped setups (see experiments 1 & 2) or well above 100 s on slowly profiling gliders (7) or floats (8 and 9). Even on the same platform, they are dependent on the optode's orientation (5).

However, we showed that, despite their (potentially) slow time response, optodes can be successfully deployed on profiling platforms to produce meaningful data. The impact of the time response on the oxygen data can be quantified and the "true" oxygen profile can be reconstructed under suitable conditions.

In principle, we found no difference between the results from laboratory experiments (1–4) and field applications (5–9), and findings are transferable between artificial step response experiments and small and continuous in situ gradients.

The main influence factor on the time response is the flow around the sensor spot, followed by temperature.

In the laboratory (1), an indirect proportionality was found for the time response and the flow rate (Fig. 4). In the field, however, no strict functional behavior was discernible, but the inverse relation is clear (see, e.g., Fig. 6c).

For the temperatures found in the ocean, a close to linear temperature effect on the response time τ was found at set flow conditions (experiments 2–4; Fig. 5, left column). This is caused by the temperature dependence of molecular diffusion, i.e., variations in oxygen diffusivity $D(T)$ and solubility $S(T)$ both in the aqueous boundary layer and in the sensing material.

In fact, boundary layer effects are a significant portion of the sensor's time response in water and must not be neglected. The manufacturers' specifications (Table 1) could be confirmed for the Aanderaa optodes using a thoroughly stirred setup (3) and for the Sea-Bird SBE63 optode using a pumped setup (2). For the JFE Alec Co. Rinko, however, response times τ were an order of magnitude higher than given by the manufacturer (τ = 0.4 s in the gas phase, JFE Alec Co. 2009) in all of our experiments due to boundary layer effects always present in water.

Using a two-layer diffusional model made up of a sensing membrane layer and a stagnant, immobile liquid boundary layer on top (Fig. 1), combined with parameterizations for $D(T)$, $S(T)$, and Fickian diffusion (*see* "Appendix"), the temperature dependence of the sensor time response vanishes (Fig. 5, right column). Instead, the liquid boundary layer thickness $l_L$ is independent of temperature and can thus be used to characterize the flow regime.

Fig.!11 gives the relation between boundary layer thickness $l_L$, temperature $T$, and response time τ for both a silicone sensing membrane with 100 µm thickness (a) and one with 50 µm thickness (b). They represent the model membrane thicknesses $l_M$ typical for an Aanderaa optode standard and fast response foil, respectively.

No such chart could be produced for the Rinko dissolved oxygen sensor due to lack of information about the sensing material thickness. Since the intended use of the Sea-Bird SBE63 is a pumped mode with set flow rate, no chart for $l_M$ = 130 µm is given but readers are referred to experiment 2 (Fig. 5a).

The look up charts of Fig. 11 can be used in two ways: (a) to characterize the flow regime ($l_L$) if a response time τ measurement exists and (b) to predict the response time τ if the flow regime ($l_L$) is known.

It, therefore, provides a tool to predict the time response for a given application. With knowledge of the sensor's response behavior, its impact on data accuracy and quality can be quantified as well as the original $O_2$ profile reconstructed (e.g., Fig. 7).

The results can be used by the community to refine thresholds for response times τ to be achieved by manufacturers, with the aim to yield scientifically usable data (see Gruber et al. 2010)

We found typical $l_L$ regimes for CTDs to be between 20 – 50 µm, depending on the CTD velocity (e.g., +1 dbar $s^{-1}$ downcast versus near-stationary or slow upcast) and sensor attachment (experiments 5 and 6).

Similarly, a boundary layer thickness $l_L$ around 90 µm was observed on a glider (7), and around a few hundred microme-

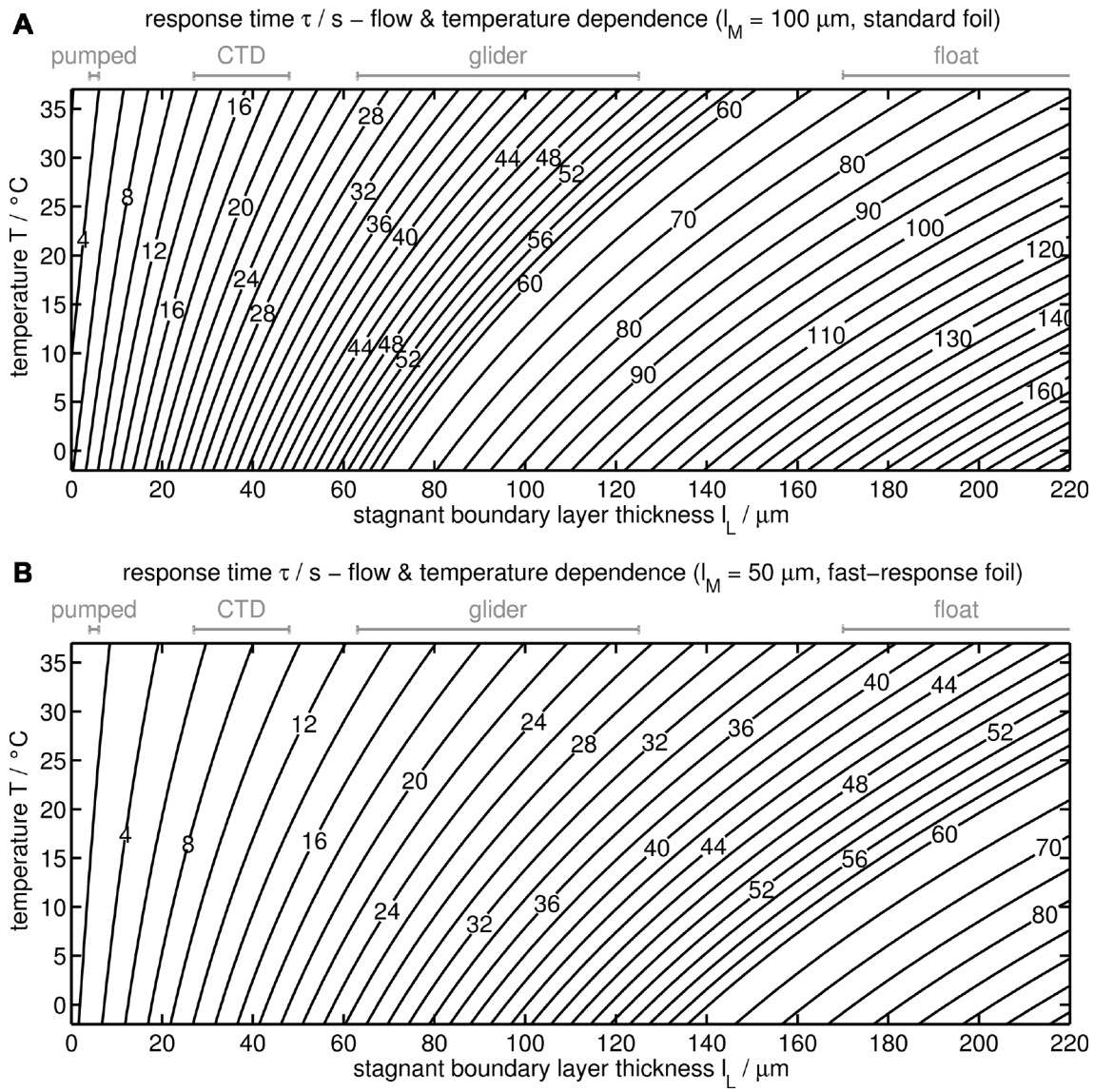


**Fig. 11.** Response time τ as a function of stagnant boundary layer thickness $l_L$ and temperature $T$ for a silicone sensing membrane with thickness $l_M$ = 100 µm (a) and $l_M$ = 50 µm (b). These thicknesses relate to model $l_M$ typical for an Aanderaa optode standard foil and a fast response foil, respectively. Gray bars denote the approximate regime for different field deployments. (For clarity, the spacing of the contour lines changes from 2 s to 5 s at τ = 60 s).

ters on floats (8 & 9). The latter two estimates are based on few observations only and need to be confirmed by further work. However, they indicate the magnitude to be expected on these important new platforms.

In addition, Fig. 11 mirrors the interplay between turbulent and molecular transport. Because the two-layer diffusional model considers only molecular diffusion, $l_L$ can be seen as a parameter of turbulent transport: exclusively turbulent transport at $l_L \to 0$ and only molecular transport at $l_L \to \infty$. Moreover, the temperature effect on τ is solely due to molecular transport, i.e., $D(T)$ and $S(T)$ variations, whereas $l_L$ proved to be temperature-independent (experiments 1–4).

In consequence, temperature becomes an important factor for τ at high $l_L$ conditions (right part of Fig. 11) such as during the float experiments 8 and 9.

Concluding this work, the time response of optical oxygen sensors has been thoroughly investigated and characterized, both in laboratory and field experiments. Whereas the two-layer diffusional model is not a completely accurate model of the hydrodynamics around the optical-sensing membrane, it provides a comprehensive and coherent picture of the main processes as well as a useful, quantitative description of the time response.

Our results can be used to assess and predict the effect on observational data even before a deployment, as well as to reconstruct an unbiased profile from field data and thus recover some of the information lost by the time response as illustrated in Fig. 7. A precondition is to know the in situ

response time τ, which can be found in this work (see Fig. 5a and 11) for typical deployment regimes. We hope this will contribute to improvements in $O_2$ data quality, especially from new ocean observatories as the Argo-$O_2$ program (Gruber et al. 2010).

## Recommendations

Based on our work, the following aspects should be considered for field applications.

(I) Whenever possible, optodes should be used in a pumped mode to achieve the smallest possible response times τ.

Having a small response time τ in the first place reduces the time response impact on the data (Eq. 8) and thus the need to reconstruct an original oxygen series. At the same time, the pumped mode represents the most reproducible mode of operation, thus minimizing uncertainties on τ for such a reconstruction. However, constraints of the deployment platform (especially battery capacity) may prevent the use of a pumped system.

(II) The sample interval should be significantly shorter than the response time τ to resolve gradient regions and to be able to reconstruct the true oxygen profile.

Especially for irregularly spaced data, e.g., on floats, the aspect of a sufficient sample interval – response time ratio should be considered: By increasing the sample frequency in gradient regions, i.e., the oxycline, a reconstruction of an unbiased and accurate field record may be feasible even with high response times.

(III) Strong gradients or high response times τ may be counterbalanced by small cast velocities (Eq. 8).

The time response impact depends on the platform's progression through water mass gradients. So even with high response times τ, the measurement error may still be acceptable if the velocities are small (e.g., experiment 9). This might be an interesting option for, e.g., moored profilers.

## Acknowledgments

The authors want to thank the captains, crew, and scientists of R/V *Polarstern* ANT-XXVII/2, R/V *Maria S. Merian* MSM 18/3, and MSM 22 as well as of R/V *Oceania* AREX10 and R/V *Islândia*. Special thanks go to Sascha Heitkam (TU Dresden, Dresden/Germany) for fruitful discussions and comments on boundary layers and fluid mechanics. Support by Gerd Rohardt (AWI, Bremerhaven/Germany) and Sebastian Milinski (GEOMAR, Kiel/Germany) with the CTD data processing of the R/V *Polarstern* and R/V *Islândia* cruises is gratefully acknowledged. Many thanks go to Jostein Hovdenes (AADI, Bergen/Norway) for valuable feedback on their sensors and Norge Larson (Sea-Bird, Bellevue/USA) for early access to and feedback on their sensor, as well as to an anonymous reviewer for valuable comments on signal processing. Financial support by the following projects is gratefully acknowledged: O2-Floats (KO 1717/3-1) and the SFB754 of the German Science Foundation (DFG) as well as the projects SOPRAN (03F0611A and 03F0462A) and HGF-CV-Station (03F0649A) of the German Research Ministry (BMBF).

## Appendix

**Sensor calibrations**

The Aanderaa optodes and the Sea-Bird SBE63 used for the laboratory experiments 1–4 were individually multi-point calibrated in the laboratory according to Bittig et al. (2012). The JFE Alec Co. Rinko (4) used the factory calibration which was validated against the other sensors. For the CTD experiments 5 and 6 and the polar float experiment 8, the Aanderaa optodes were as well multi-point calibrated in the laboratory (Bittig et al. 2012) and their data validated against in situ Winkler samples. The Rinko sensor of 5 used the factory calibration coefficients and was calibrated in situ against Winkler samples. The same applies to the Aanderaa optode of experiment 9. The Aanderaa optode of experiment 7 was in situ calibrated before being mounted on the glider. For this, the optode was attached to the CTD frame for a calibration cast. Bottle stops were about 120 s long and Winkler samples as well as data from a Winkler-calibrated SBE43 were used to calibrate the optode (see Hahn 2013).

**Two-layer diffusional model**

The model applied to our data is inspired by Linek et al. (2009). They extended a one-layer model of Cox and Dunn (1986) to include a stagnant boundary layer.

Cox and Dunn (1986) used a planar geometry of a luminophore-doped silicone membrane to derive oxygen diffusion coefficients. Their diffusional model is based on Fickian diffusion (Eqs. 9 and 10), an impermeable boundary at the optical window-side of the sensing membrane (Eq. 11), and a bulk environment assumed to be sufficiently large and well mixed to be considered as infinite, unaffected reservoir (Eq. 12). It uses Eq. 13 as initial condition and considers only one layer, the silicone membrane with thickness $l_M$. The materials are assumed to be homogenous (uniform $D$ and $S$) and normalized space ($X = x/l_M$) and partial pressure ($\Phi = pO_2/pO_{2,\infty}$) coordinates are used. In addition, temporal temperature variations are assumed to be small enough to neglect the temperature dependence of $D$ and $S$.

$$J = -D\frac{\partial\Phi(x,t)}{\partial x} \tag{9}$$

$$\frac{\partial\Phi(x,t)}{\partial t} = D\frac{\partial^2\Phi(x,t)}{\partial x^2} \tag{10}$$

$$\frac{\partial\Phi(x,t)}{\partial x} = 0 \qquad x = 0,\ t \geq 0 \tag{11}$$

$$\Phi(x,t) = 1 \qquad x = \text{bulk},\ t \geq 0 \tag{12}$$

$$\Phi(x,t) = 0 \qquad t = 0 \tag{13}$$

Analogous differential equations have been solved for the conduction of heat decades ago (Carslaw and Jaeger 1976) and the solution from Crank (1975) is given in Eq. 14.

$$\Phi(X,t) = 1 - \frac{4}{\pi}\sum_{n=0}^{\infty}\left[\frac{(-1)^n}{2n+1}\cdot e^{-\frac{(2n+1)^2}{4}\pi^2\frac{D_M}{l_M^2}\cdot t}\cdot\cos\left(\frac{2n+1}{2}\pi\cdot X\right)\right] \quad (14)$$

The time response of the sensor $h(t)$ is assumed to be the integral of the entire sensing membrane ($0 \le x \le l_M$) according to Eq. 15.

$$h(t) = \overline{\Phi_M} = \int_0^1 \Phi(X,t)\,\mathrm{d}X = \int_0^{l_M} \Phi(x,t)\,\mathrm{d}x \quad (15)$$

The thus obtained step response for the one-layer model of Cox and Dunn (1986) is given in Eq. 16 and shown in Fig.!12b.

$$h(t) = 1 - 8\sum_{n=0}^{\infty}\left[\frac{1}{(2n+1)^2\,\pi^2}\cdot e^{-\frac{(2n+1)^2}{4}\pi^2\frac{D_M}{l_M^2}\cdot t}\right] \quad (16)$$

The one-layer model has its representation, e.g., as a gas phase step response experiment ($N_2$ gas ↔ air) (*see* JFE Alec Co. 2009).

The two-layer model of Linek et al. (2009) contains a silicone membrane (thickness $l_M$) as before. They added an immobile, stagnant liquid boundary layer (thickness $l_L$) with additional boundary conditions at the layers' interface (continuity of Φ and $J$: Eqs. 17 and 18) and adjusting Eq. 10 according to the regime of the layer (Eqs. 19 and 20).

$$\begin{aligned}\left(\Phi(x,t)\right)_{x\to l_{M^-}} &= \left(\Phi(x,t)\right)_{x\to l_{M+}} \qquad t \ge 0\\ \left(J(x,t)\right)_{x\to l_{M^-}} &= \left(J(x,t)\right)_{x\to l_{M+}} \qquad t \ge 0\end{aligned} \quad (17)$$

$$D_M\left(\frac{S_M\cdot\partial\Phi(x,t)}{\partial x}\right)_{x\to l_{M^-}} = D_L\left(\frac{S_L\cdot\partial\Phi(x,t)}{\partial x}\right)_{x\to l_{M+}} \qquad t \ge 0 \quad (18)$$

$$\frac{\partial\Phi(x,t)}{\partial t} = D_M\frac{\partial^2\Phi(x,t)}{\partial x^2} \qquad 0 \le x \le l_M \quad (19)$$

$$\frac{\partial\Phi(x,t)}{\partial t} = D_L\frac{\partial^2\Phi(x,t)}{\partial x^2} \qquad l_M \le x \le l_L \quad (20)$$

For the normalized partial pressure Φ, the authors give Eq. 21 as solution to the system of differential equations.

$$\Phi(X,t) = 1 - \sum_{n=0}^{\infty} Q_n\cdot\nu_n(X)\cdot e^{-\lambda_n\frac{D_M}{l_M^2}\cdot t} \qquad 0 \le X \le \frac{l_M + l_L}{l_M} \quad (21)$$

It makes use of

$$\nu_n(X) = \cos(\lambda_n X) \qquad 0 \le X \le 1 \quad (22)$$

$$\nu_n(X) = \frac{\cos\lambda_n}{\sin(A_L\,\lambda_n)}\sin\left(\sqrt{\frac{D_M}{D_L}}\lambda_n\left(\frac{l_L - l_M}{l_M} - X\right)\right) \qquad 1 \le X \le \frac{l_M + l_L}{l_M} \quad (23)$$

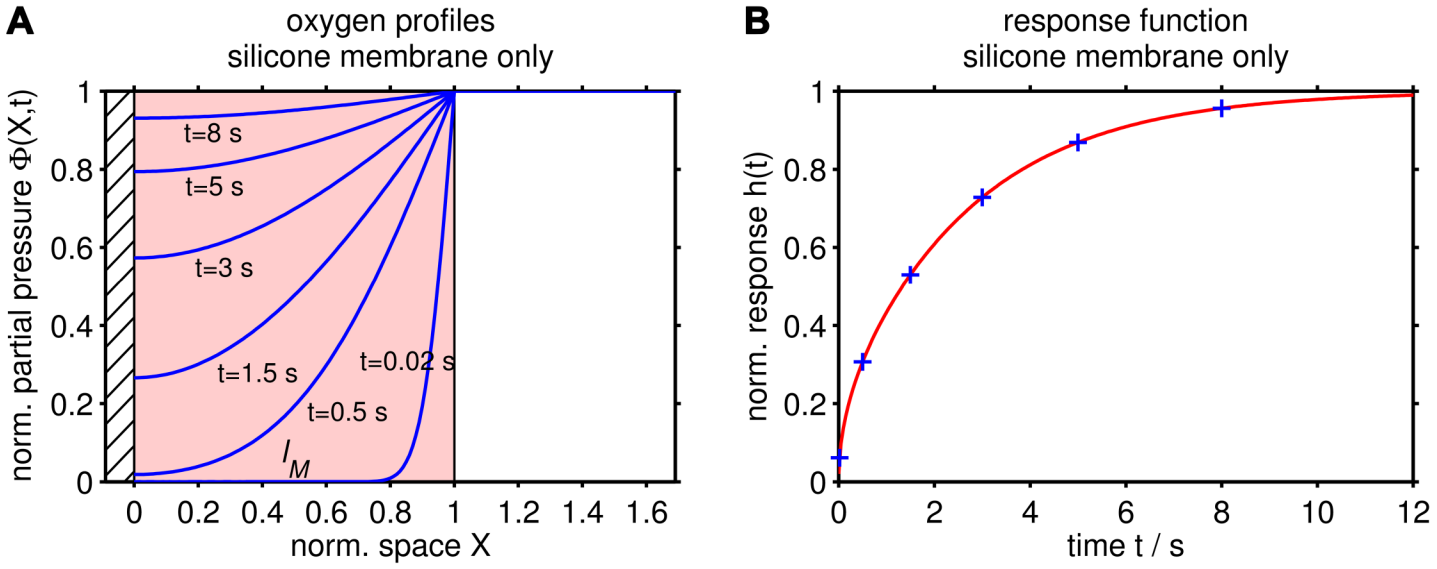


**Fig. 12.** One-layer diffusional optode model consisting of a silicone membrane ($0 \le X \le 1$) with impermeable boundary (hatched, optical window) after Cox and Dunn (1986). (a) Oxygen profiles inside the membrane after an ambient step change in normalized partial pressure $\Phi(X > (l_M + l_L)/l_M, t = 0)$ from 0 to 1. (b) Step response $h(t)$ of the optode. A membrane thickness of $l_M$ = 100 μm (Aanderaa optode standard foil) and material properties according to Table 4 were used.

and

$$Q_n = \frac{2}{\lambda_n} \frac{\cos(\lambda_n)\,\sin(A_L\,\lambda_n)}{K_L\,\sin^2(A_L\,\lambda_n) + A_L\,\cos^2(\lambda_n)} \quad (24)$$

where $\lambda_n$ denotes the n-th positive root of the eigenvalue equation

$$K_L\,\sin(\lambda_n)\,\sin(A_L\,\lambda_n) - \cos(\lambda_n)\,\cos(A_L\,\lambda_n) = 0 \quad (25)$$

governed by the dimensionless parameters $A_L$, $K_L$, and $L_L$ :

$$A_L = \frac{l_L\,\sqrt{D_M}}{l_M\,\sqrt{D_L}} \quad (26)$$

$$L_L = \frac{l_L\,D_M\,S_M}{l_M\,D_L\,S_L} \quad (27)$$

$$K_L = \frac{\sqrt{D_M}\,S_M}{\sqrt{D_L}\,S_L} = \frac{L_L}{A_L} \quad (28)$$

The step response of the sensor membrane is given by Eq. 29 for the two-layer model (Linek et al. 2009).

$$h(t) = 1 - \sum_{n=0}^{\infty} \frac{Q_n}{\lambda_n} \sin(\lambda_n)\; e^{-\lambda_n^2 \frac{D_M}{l_M^2} \cdot t} \quad (29)$$

Again, Eq. 21 determines the $O_2$ profiles or partial pressure distribution, respectively. It is illustrated for a 100 μm thick silicone membrane (standard foil) and a 60 μm stagnant boundary layer in Fig. 1a. The sensor's step response $h(t)$ (Eq. 29) is shown in Fig. 1b for different stagnant boundary layer thicknesses.

Eq. 29 has been used to quantify the laboratory results (1 – 4), using the boundary layer thickness $l_L$, an amplitude $A$, and a time offset $t_0$ as fit parameters (analogous to the exponential approach, see Eq. 3).

In fact, the exponential approach is a (strong) simplification of the diffusional model: The scale factor in both equation 16 and 29, $1/(2n+1)^2$ and $Q_n/\lambda_n \sin(\lambda_n)$, respectively, decreases rapidly with increasing index n. At the same time, the factor in the exponential grows proportional to $n^2$. That causes the leading term ($n = 0$) to dominate $h(t)$ except right at the start ($t \to 0$).

Model parameters and material properties are summarized in Table!4. An Arrhenius-type relation was used for the silicone membrane's diffusivity $D(T)$ and solubility $S(T)$ while empirical equations were applied for the liquid layer (Holmén and Liss 1984; Garcia and Gordon 1992).

In reality, fluid dynamics differ to some considerable extent with sensor shape (flow field close to the sensing membrane) and deployment mode (flow field around the sensor) and a full description would require the simulation of flows and mass transfer for each case. This includes different shapes and builds of the same sensor model, e.g., the Aanderaa optode model 3830. The stagnant boundary layer model thus has its limitations, but serves as a useful and comprehensive tool to characterize the time response behavior apart from a phenomenological response time τ.

**Table 4.** Material properties and membrane thickness $l_M$ used for the two-layer diffusional model.

| Property | Value | Source |
|---|---|---|
| $D_M$ (25°C) / m² s⁻¹ | 1.48 × 10⁻⁹ | Robb (1968) |
| $E_D$ / kJ mol⁻¹ | 20.0 | Cox and Dunn (1986) |
| $S_M$ (25°C) / mol m⁻³ Pa⁻¹ | 13.15 × 10⁻⁵ | Robb (1968) |
| $E_S$ / kJ mol⁻¹ | –12.6 | Cox and Dunn (1986) |
| $D_L$ (25°C) / m² s⁻¹ | 2.31 × 10⁻⁹ | Holmén and Liss (1984) |
| $S_L$ (25°C) / mol m⁻³ Pa⁻¹ | 1.22 × 10⁻⁵ | Garcia and Gordon (1992) |
| $l_M$ (3830 and 4330) / μm | 100 | Huber (2010) |
| $l_M$ (4330F) / μm | 50 | $l_t^\infty$ extrapolation (1) |
| $l_M$ (SBE63) / μm | 130 | $l_t^\infty$ extrapolation (1) |

**Filter discretization**

The exponential step response $h(t)$ given by Eq. 3 with a single time constant yields the impulse response $\dot{h}(t)$

$$\dot{h}(t) = \frac{\mathrm{d}}{\mathrm{d}t} h(t) = \frac{1}{\tau} \cdot e^{-\frac{t}{\tau}} \quad (30)$$

Its LaPlace transform

$$H(\mathrm{s}) = \frac{1}{1 + \mathrm{s} \cdot \tau} \quad (31)$$

is a single-pole low-pass filter with $\mathrm{s} = j\,2\pi\mathrm{f}$ being the LaPlace variable and f the frequency. The LaPlace transformation translates the continuous time-domain response, $\dot{h}(t)$, to the frequency-domain transfer function, $H(\mathrm{s})$, of the filter.

The bilinear transformation can be used to approximate the continuous filter in the discrete-time domain. It equates integration in the continuous domain with integration by the trapezoidal rule in the discrete domain. The relationship between continuous-time $H(\mathrm{s})$ and discrete-time transfer function $H(z)$ is given by

$$\mathrm{s} = \frac{2}{\Delta t} \cdot \frac{z-1}{z+1} \quad (32)$$

where $z = \exp(j\,2\pi\mathrm{f}\,\Delta t)$ and $\Delta t$ is the sample interval. Substituting Eq. 32 into the LaPlace transform (Eq. 31) gives

$$H(z) = \frac{b \cdot (1 + z^{-1})}{1 - a \cdot z^{-1}} \quad (33)$$

with

$$b = \left(1 + 2\frac{\tau}{\Delta t}\right)^{-1} \qquad a = 1 - 2b \quad (34)$$

The discrete realization of the *Z*-transform $H(z)$ is

$$c_{i+1}^{\text{filt}} = a \cdot c_i^{\text{filt}} + b \cdot \left( c_{i+1}^{\text{in situ}} + c_i^{\text{in situ}} \right) \tag{35}$$

which is equal to Eq. 4.

Compared with "simpler" discrete realizations like, e.g.,

$$c_{i+1}^{\text{filt}} = c_i^{\text{filt}} + \left( c_i^{\text{in situ}} - c_i^{\text{filt}} \right) \cdot \left( 1 - e^{-\frac{\Delta t}{\tau}} \right) \tag{36}$$

the bilinear transformation has the advantage that its phase is independent of the $\Delta t/\tau$ ratio, which is not true for Eq. 36.

**Field data analysis**

The 95% confidence intervals of the fit parameters $\tau$ and $r$ were used as quality control: Only when the response time $\tau$ was determined to better than ± 5 s and the calibration offset $r$ to better than ± 2 μmol kg$^{-1}$ the fit was considered appropriate and rejected otherwise. This ensures that only those observations are retained, where both the optode and the reference showed a time response (i.e., observations near gradients).

The results of the field experiments 5–7 were interpreted statistically by using an inverse Gaussian distribution. For experiments 8 and 9, however, only simple statistics are presented as the number of observations is too limited.

The inverse Gaussian describes the time distribution for Brownian diffusion along a gradient for a set distance and is skewed toward high values. The frequency distribution of the Aanderaa optode in situ response times for experiment 5 is shown in Fig.!13 and proved to be appropriately described by this kind of distribution.

For interpretation, the in situ data were binned into both CTD vertical velocity and temperature bins and the bins fitted individually. For clarity, only the mode value, width (mean ± σ), and mean value of the fitted distribution are given in the figures. In addition, only bins with at least 2% of the total sample size are shown to ensure statistical robustness. For the same reason, the mean values and standard deviations are based on the fitted distribution to reduce the impact of high $\tau/I_L$ outliers.

**Reconstruction algorithm**

The main concern of inverse filtering is the amplification of noise in the data. This is an issue especially close to strong gradients, where spurious spikes are introduced easily.

The algorithm after Miloshevich et al. (2004) works both with regularly spaced data (e.g., CTD, glider) as well as with irregularly spaced data (e.g., float) and assumes the true profile to be inherently smooth. We applied a two-step procedure, first smoothing the measurements with a ± 0.2 μmol kg$^{-1}$ tolerance and then applying the time-lag correction.

The smoothing algorithm is derivative-based and tries to reduce changes in curvature by displacing the data points within the given tolerance, thus creating a locally smooth data series. Their time-lag correction inverts Eq. 36 which requires $\Delta t$ to be an order of magnitude smaller than $\tau$ to give the correct phase.

The direct inversion of the bilinear transform (Eq. 35) would be more suitable, but is prone to strong oscillations in the reconstructed profile even with small measurement errors

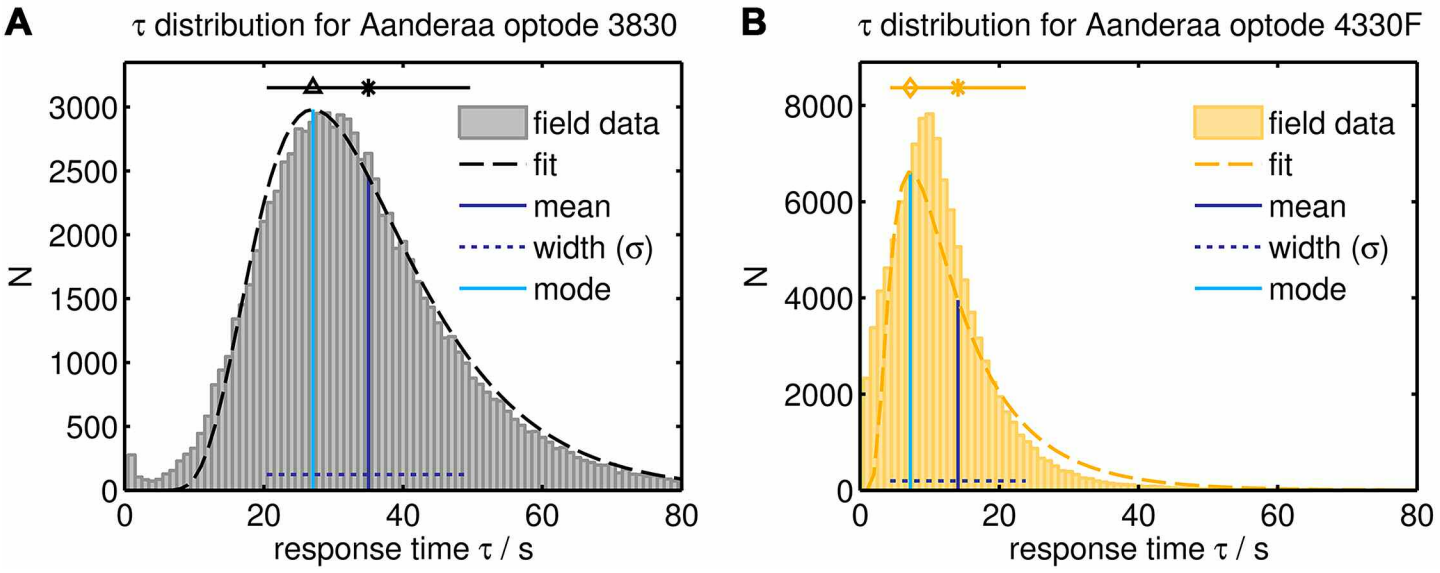


**Fig. 13.** Distribution of response times τ obtained from in situ data for the entire R/V *Polarstern* cruise ANT-XXVII/2 (5) for Aanderaa optode model 3830 (a) and model 4330F (b). The colored histogram shows the field data and the dashed line the fitted inverse Gaussian distribution. The distribution's mean value (blue line), width (mean ± σ, dotted blue line), and mode value (cyan line) are given. These three parameters are used to describe the skewed distribution in the other figures using the shorthand (asterisk, bar, and marker) depicted at the top.

and would require an additional averaging step. However, rearranging Eq. 35 to

$$\frac{c_{i+1}^{\text{in situ}} + c_i^{\text{in situ}}}{2} = \frac{1}{2b} \cdot \left( c_{i+1}^{\text{filt}} - a \cdot c_i^{\text{filt}} \right) \quad (37)$$

shows that the mean of consecutive data points of the "true" profile $c^{\text{in situ}}$ is directly accessible from the measurements $c^{\text{filt}}$, because the bilinear transformation equates integration between $t_i$ and $t_{i+1}$ with the trapezoidal rule. This profile of consecutive means can be interpolated to the original measurement times, and in fact, gives a result similar to the Miloshevich et al. (2004) approach but with correct phase (root-mean-square error of 3.6 μmol kg$^{-1}$ for the CTD profile of Fig. 7).

## Nomenclature

| | |
|---|---|
| $I$ | luminescence intensity in the presence of $O_2$ |
| $I_0$ | luminescence intensity in the absence of $O_2$ |
| $\Lambda$ | luminophore excited state lifetime in the presence of $O_2$ / s |
| $\Lambda_0$ | luminophore excited state lifetime in the absence of $O_2$ / s |
| $K_{SV}$ | Stern-Volmer constant of the luminophore / Pa$^{-1}$ |
| $pO_2$ | partial pressure of oxygen / Pa |
| $c(O_2)$ | concentration of oxygen / μmol kg$^{-1}$ |
| $\alpha(O_2)$ | Henry's law oxygen solubility constant, Bunsen coefficient / μmol kg$^{-1}$ Pa$^{-1}$ |
| φ | phase shift of the sensor / ° |
| $f$ | modulation frequency of the sensor, frequency / s$^{-1}$ |
| $T$ | temperature / °C |
| $t$ | (elapsed) time / s |
| τ | response time / s |
| $D_i(T)$ | diffusivity in layer $i$ / m$^2$ s$^{-1}$ |
| $\nu$ | kinematic viscosity of water / m$^2$ s$^{-1}$ |
| $Sc$ | Schmidt number $Sc = \nu/D$, dimensionless |
| $S_i(T)$ | solubility in layer $i$ / mol m$^{-3}$ Pa$^{-1}$ |
| $l_i$ | thickness of layer $i$ / m |
| $h(t)$ | normalized step response function, dimensionless |
| $x$ | space coordinate, location / m |
| $X$ | normalized space coordinate $x = x/l_M$, dimensionless |
| $\Phi(x,t)$ | normalized partial pressure $\Phi(x,t) = pO_2/pO_{2,\infty}$, dimensionless |
| $A$ | step height amplitude for exponential model (Eq. 3) / μmol kg$^{-1}$ |
| $t_0$ | time offset for exponential model (Eq. 3) / s |
| $a$ | parameter of the bilinear $Z$-transform (Eq. 4), dimensionless |
| $b$ | parameter of the bilinear $Z$-transform (Eq. 4), dimensionless |
| $f_0$ | initial forcing/initial condition for the filter (Eq. 5) / μmol kg$^{-1}$ |
| $r$ | calibration offset between $c^{\text{in situ}}$ and $c^{\text{SBE43}}$ (Eq. 6) / μmol kg$^{-1}$ |
| σ | standard deviation |
| $\beta_i$ | measurement error due to time response $h(t)$ at $t_i$ / μmol kg$^{-1}$ |
| $\delta_i$ | local forcing, impulse on β at $t_i$ / μmol kg$^{-1}$ |
| $p$ | hydrostatic pressure / dbar |
| $s$ | flow speed, vertical velocity $s = dp/dt$ / dbar s$^{-1}$ |
| $g$ | oxygen gradient $g = dc/dp$ / μmol kg$^{-1}$ dbar$^{-1}$ |
| $J(x,t)$ | particle flux / mol m$^{-2}$ s$^{-1}$ |
| $\nu_n$, $Q_n$, $\lambda_n$ | expressions after Eq. 22–25, dimensionless |
| $A_L$, $L_L$, $K_L$ | parameters after Eq. 26–28, dimensionless |
| $E_D$ | activation energy of diffusion of $O_2$ in silicone / kJ mol$^{-1}$ |
| $E_S$ | solution enthalpy of $O_2$ in silicone / kJ mol$^{-1}$ |
| $\dot{h}(t)$ | impulse response function / s$^{-1}$ |
| $H$ | filter transfer function, dimensionless |
| s | LaPlace variable / s$^{-1}$ |
| $z$ | (complex) variable of the $Z$-transform $z = e^{s\,\Delta t}$, dimensionless |
| in situ | in situ value |
| SBE43 | SBE43 measured value |
| filt | filtered/response time influenced value |
| optode | optode measured value |
| $M$ | index to sensing membrane |
| $L$ | index to boundary layer |

## References

Aanderaa Data Instruments AS. 2012. Oxygen optode 4330/4330F data sheet. Bergen, Norway.

Bittig, H. C., B. Fiedler, T. Steinhoff, and A. Körtzinger. 2012. A novel electrochemical calibration setup for oxygen sensors and its use for the stability assessment of Aanderaa optodes. Limnol. Oceanogr. Methods 10:921-933 [doi:10.4319/lom.2012.10.921].

Carslaw, H. S., and J. C. Jaeger. 1976. Conduction of heat in solids, 2 ed. Clarendon Press.

Cox, M. E., and B. Dunn. 1986. Oxygen diffusion in poly(dimethyl siloxane) using fluorescence quenching. I. Measurement technique and analysis. J. Polym. Sci. A24:621-636 [doi:10.1002/pola.1986.080240405].

Crank, J. 1975. The mathematics of diffusion, 2 ed. Clarendon Press.

Demas, J. N., B. A. DeGraff, and P. B. Coleman. 1999. Oxygen sensors based on luminescence quenching. Anal. Chem. 71:793A-800A [doi:10.1021/ac9908546].

Edwards, B., D. Murphy, C. Janzen, and N. Larson. 2010. Calibration, response, and hysteresis in deep-sea dissolved oxygen measurements. J. Atmos. Oceanic Technol. 27:920-931 [doi:10.1175/2009JTECHO693.1].

Fiedler, B., P. Fietzek, N. Vieira, P. Silva, H. C. Bittig, and A. Körtzinger. 2013. In situ $CO_2$ and $O_2$ measurements on a profiling float. J. Atmos. Oceanic Technol. 30:112-126 [doi:10.1175/JTECH-D-12-00043.1].

Garcia, H. E., and L. I. Gordon. 1992. Oxygen solubility in seawater: Better fitting equations. Limnol. Oceanogr. 37:1307-1312 [doi:10.4319/lo.1992.37.6.1307].

Gruber, N., and others. 2010. Adding oxygen to Argo: Developing a global in-situ observatory for ocean deoxygenation and biogeochemistry. *In* J. Hall, D. E. Harrison, and D. Stammer [Eds.], Proceedings of OceanObs'09: Sustained ocean observations and information for society. ESA Publication WPP-306, Venice, Italy, 21-25 September 2009. Volume 2 [doi:10.5270/OceanObs09.cwp.39].

Hahn, J. 2013. Oxygen variability and eddy-driven meridional oxygen supply in the tropical North East Atlantic oxygen minimum zone. Ph.D. thesis, Universität Kiel.

Holmén, K., and P. Liss. 1984. Models for air-water gas transfer: an experimental investigation. Tellus 36B:92-100 [doi:10.1111/j.1600-0889.1984.tb00231.x].

JFE Alec Co. 2009. RINKO fast-optical oxygen sensor data sheet. Kobe, Japan. Rev. Oct. 6, 2009.

Johnson, K. S., J. A. Needoba, S. C. Riser, and W. J. Showers. 2007. Chemical sensor networks for the aquatic environment. Chem. Rev. 107:623-640 [doi:10.1021/cr050354e].

Klimant, I., V. Meyer, and M. Kühl. 1995. Fiber-optic oxygen microsensors, a new tool in aquatic biology. Limnol. Oceanogr. 40:1159-1165 [doi:10.4319/lo.1995.40.6.1159].

Körtzinger, A., J. Schimanski, and U. Send. 2005. High quality oxygen measurements from profiling floats: A promising new technique. J. Atmos. Oceanic Technol. 22:302-308 [doi:10.1175/JTECH1701.1].

Krahmann, G., and T. Fischer. 2012. Physical oceanography during Maria S. Merian cruise MSM18/3. IFM-GEOMAR Leibniz-Institute of Marine Sciences, Kiel University. Pangaea.

Linek, V., T. Moucha, M. Kordac, M. Dubcová, F. Hovorka, and J. Rejl. 2009. Liquid film effect on dynamics of optical oxygen probe. Comparison with polarographic oxygen probes. Diffusion coefficients measuring technique. Chem. Eng. Sci. 64:4005-4015 [doi:10.1016/j.ces.2009.06.015].

Miloshevich, L. M., A. Paukkunen, H. Vömel, and S. J. Oltmans. 2004. Development and validation of a time-lag correction for Vaisala radiosonde humidity measurements. J. Atmos. Oceanic Technol. 21:1305-1327 [doi:10.1175/1520-0426(2004)021<1305:DAVOAT>2.0.CO;2].

Robb, W. L. 1968. Thin silicone membranes—Their permeation properties and some applications. Ann. N.Y. Acad. Sci. 146:119-137 [doi:10.1111/j.1749-6632.1968.tb20277.x].

Rohardt, G., E. Fahrbach, and A. Wisotzki. 2011. Physical oceanography during POLARSTERN cruise ANT-XXVII/2. Alfred Wegener Institute, Helmholtz Center for Polar and Marine Research. Pangaea.

Rosner, B. 1983. Percentage points for a generalized ESD many-outlier procedure. Technometrics 25:165-172 [doi:10.2307/1268549].

Schlichting, H., and K. Gersten. 1997. Grenzschicht-Theorie, 9 ed. Springer.

Sea-Bird electronics. 2012. SBE63 Optical dissolved oxygen sensor brochure. <http://www.seabird.com/products/spec_sheets/63data.htm>.

Tengberg, A., and others. 2006. Evaluation of a lifetime-based optode to measure oxygen in aquatic systems. Limnol. Oceanogr. Methods 4:7-17 [doi:10.4319/lom.2006.4.7].

Uchida, H. 2010. High-quality oxygen measurements by using fast-responding optode sensors. *In* Aoyama, M., Hydes, D. Daniel, A., Bakker, K., Murata, A., Tanhua, T. and Woodward, E. M. S. First Meeting of the joint IOC-ICES Study Group on Nutrient Standards (SGONS); IOC Reports of Meetings of Experts and Equivalent Bodies, 223. UNESCO 2010. <http://unesdoc.unesco.org/images/0018/001881/188100e.pdf>

*Submitted 10 December 2013*
*Revised 27 May 2014*
*Accepted 23 July 2014*